Dynamical and Rheological Properties of Soft Colloid Suspensions

Roland G. Winkler, Dmitry A. Fedosov, and Gerhard Gompper*

Theoretical Soft Matter and Biophysics, Institute of Complex Systems and Institute for Advanced Simulation, Forschungszentrum Jülich, D-52425 Jülich, Germany

Abstract

Soft colloids comprise a wide class of materials, ranging from linear polymers over polymeric assemblies, such as star polymers and dendrimers, to vesicles, capsules, and even cells. Suspensions of such colloids exhibit remarkable responses to imposed flow fields. This is related to their ability to undergo conformational changes and elastic deformations, and the adaptation of their dynamical behavior. The rational design of soft particles for targeted applications or the unraveling of their biological function requires an understanding of the relation between their microscopic properties and their macroscopic response. Here, mesoscale computer simulations provide an invaluable tool to tackle the broad range of length and time scales. In this article, we discuss recent theoretical and simulation results on the rheological behavior of ultrasoft polymeric colloids, vesicles, capsules, and cells. The properties of both, individual particles and semi-dilute suspensions, are addressed.

Keywords: Ultrasoft colloids, polymers, star polymers, dendrimers, vesicles, cells, blood cells, capsules, elasticity, deformability, dynamics, tumbling, tank-treading, rheology, viscosity, shear thinning

1. Introduction

The theoretical understanding of the rheological properties of colloidal suspensions started in 1906, more than a hundred years ago, with the now classical paper [1] of Albert Einstein, in which he predicted the viscosity η of a suspension of hard spheres to depend on the volume fraction Φ to leading order as

$$\eta = \eta_s \left[1 + \frac{5}{2}\Phi + O(\Phi^2) \right], \tag{1}$$

where η_s is the solvent viscosity. This result has turned out to be extremely useful, in particular because it does not only apply to hard spheres in the regime of $\Phi \lesssim 0.1$, but also to much more flexible objects like coiled linear polymers, when an appropriate radius of the coil, the "hydrodynamic radius" R_H, is employed to determine the volume fraction.

This raises the question about the importance of shape and deformability of soft colloids for the rheological behavior of their suspensions. Is it sufficient to define an appropriate hydrodynamic radius and otherwise employ the theoretical description of hard spheres? What is the maximum volume fraction to which such a description might be accurate and useful? Do all soft colloids behave the same, or is the physical origin of their softness important? What is the dependence of viscosity on the elastic moduli of the soft colloids? What is the role of shape, and how do shape and deformability together determine the rheological properties of a suspension?

There is a large range of applications, in which the rheological behavior of soft-colloid suspensions plays an important role. From a technological point of view, polymer suspensions are probably the most dominant. However, even this long-studied class of materials has seen several interesting developments in recent years. For linear polymers, semi-dilute solutions have been studied in detail, and the relation of orientation and elongation of single chains to the macroscopic rheological properties has been elucidated. More importantly, polymers with a more complex architecture have been investigated, such as star polymers, dendrimers, and hyperbranched polymers.

A second class of soft objects are vesicles, capsules, and cells. Capsules are also interesting for technological applications. However, the main focus of such suspensions is in the biomedical field. Blood is a suspension of mainly red blood cells, with a volume fraction of nearly 50%. Red blood cells are of biconcave shape, and are highly deformable because they have to squeeze through the tiny vessels of microvascular network. Thus, the deformability of red blood cells, which may get reduced in diseases such as malaria or diabetes, and its effect on blood viscosity are very important for blood flow. Similarly, vesicles and capsules are used as model systems for cells, but also as drug-delivery vehicles. They may differ from cells by their shape and type of membrane elasticity, and thus show different rheological properties.

To establish a relation between the structure of soft colloids and their macroscopic rheological properties, the microscopic understanding of their non-equilibrium properties is desired. This is difficult to achieve experimentally. Here, computer simulations are the appropriate tool for microscopic insight into soft matter and bio-fluid dynamics. In particular, recently developed novel mesoscale simulation approaches provide a de-

*Corresponding author

Email address: r.winkler@fz-juelich.de, d.fedosov@fz-juelich.de, g.gompper@fz-juelich.de (Roland G. Winkler, Dmitry A. Fedosov, and Gerhard Gompper)

tailed microscopic understanding, structure-function relationships, and shed light on universal non-linear dependencies.

In general, soft colloids show much richer rheological properties than their hard counterparts [2]. This poses additional challenges for the understanding and prediction of their behavior in semi-dilute and dense suspensions. However, it also offers new opportunities in terms of applications, because the variation of particle properties implies the tunability of rheological behavior over a wide range.

2. Simulation Techniques

During the last few decades, various mesoscale simulation approaches have been developed to bridge the length- and timescale gap inherent in soft matter systems. Prominent examples are the Lattice Boltzmann method (LB) [3–5], Dissipative Particle Dynamics (DPD) [6–8], and the Multiparticle Collision Dynamics (MPC) approach [9–11], which is based on the Direct Simulation Monte Carlo (DSMC) approach [12]. Common to these approaches is a simplified, coarse-grained description of the solvent degrees of freedom in order to achieve high computational efficiency while keeping the essential features of the microscopic physics on the length scales of interest—specifically hydrodynamics. Embedded objects, such as polymers or colloids are treated by conventional molecular dynamics simulations.

2.1. Dissipative Particle Dynamics

In Dissipative Particle Dynamics (DPD), each particle represents a *molecular cluster* rather than an individual atom, and can be thought of as a soft lump of fluid. The DPD system consists of N point particles, which interact through three pairwise forces denoted as conservative, dissipative, and random forces. The conservative force controls fluid compressibility, while the dissipative force supplies fluid viscosity. The DPD system is kept at equilibrium temperature with a local thermostat, which is formed by the pair of dissipative and random forces. The time evolution of velocities and positions of particles is determined by the Newton's second law of motion.

2.2. Multiparticle Collision Dynamics

In the Multiparticle Collision Dynamics approach, the fluid is represented by a large number of point particles, which move in continuous space with a continuous distribution of velocities. Dynamically, the particles undergo alternating streaming and collision steps. In the streaming step, they move ballistically with their respective velocities for a time interval, which is denoted as collision time. Interactions between the particles appear in the collision step. Thereby, the system is coarse-grained into a grid of cubic cells, which define the collision environment. Only particles within a cell interact with each other by a momentum-conserving stochastic process, which leads to build-up of fluid correlations. Various collision rules have been proposed [9, 13, 14], however, the originally proposed Stochastic Rotation Dynamics (SRD) implementation is still preferentially used [9]. Here, the relative fluid particle velocities within a collision cell are rotated around a randomly oriented axis by a defined angle. The algorithm exhibits unconditional stability [9], incorporates thermal fluctuations and hydrodynamic interactions [15]. Since it is particle-based, the MPC method can easily be combined with other simulation approaches such as molecular dynamics simulations. Moreover, mechanical expressions can be exploited to calculate, e.g., the stress tensor [16], or to implement an appropriate temperature control [17].

2.3. Polymer Model

Typically coarse-grained models are used in simulations, where polymers are represented as bead-spring or bead-rod chains [18–21]. Stiffness is introduced by harmonic next-nearest neighbor interactions. To build a star polymer, linear polymers are connected to a common central particle. Thereby, the respective bond length might be chosen larger than that of other bonds, in order to accommodate the required particles in the core region [22, 23]. Excluded volume interactions are modeled by a truncated and shifted purely-repulsive Lennard-Jones potential.

2.4. Membrane models

Depending on a suspended particle of interest, a membrane model may need to incorporate elastic and viscous properties of a membrane, its bending resistance, and the viscosity contrast between inner and outer fluids. One class of models can be referred to as continuum approaches, where membrane properties follow some constitutive relations. For example, in-plane membrane shear elasticity can be described by Hookean or neo-Hookean law, while out-of-plane deformations are controlled by curvature elasticity [24–26]. Another class of membrane models corresponds to the network model of a membrane, which is built by a set of points which form a two-dimensional triangulated network on a membrane surface [27–32]. These models typically incorporate bending and stretching resistance, and area and volume constraints. In addition, viscoelastic membrane properties can be mediated by springs with attached dashpots [31]. These network models assume a fixed connectivity; however, there exist a network model for a fluidic membrane (e.g., used for modeling fluid vesicles) which employs a dynamically triangulated network [27, 28, 33]. The fluidic membrane combined with a fixed elastic network leads to a two-layer membrane model [28, 33]. Recently, a model of two continuous layers has been developed [34], which allows for sliding and detachment of the two corresponding layers.

In continuum methods, coupling between membrane deformation and fluid flow is often implemented through the immersed boundary method (IBM) [24, 35] or front tracking method (FTM) [25], which advect vertices with the local fluid velocity and exert membrane forces onto the fluid flow. Alternatively, fluid-structure interactions can be implemented through viscous coupling. In particle-based methods, the no-slip boundary conditions at the membrane surface are implemented through viscous force coupling in DPD [31] or collisions in MPC [28] between fluid particles and membrane vertices.

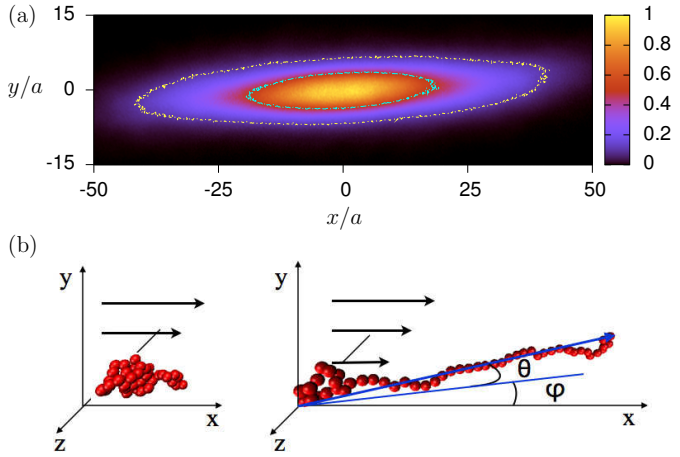

Figure 1: (a) Monomer density distribution in the flow-gradient plane for $N_p = 3000$, $N_m = 250$, i.e., $c/c^* = 10.38$, and $Wi_c = 569$. The contour lines for the densities 0.1 (outer) and 0.5 (inner) are highlighted to emphasize the non-ellipticity of the shape. (b) Illustration of polymer stretching (right) and recoiling (left). θ is the angle between the end-to-end vector and its projection onto the flow-gradient plane and φ is the angle between this projection and the flow direction. From Ref. [48].

3. Polymeric Particles

Studies of the rheological properties of polymer systems have a long history, driven by the importance of these materials in industrial applications. Correspondingly, there is a wide-range of literature on various aspects of polymer solutions and melts including experiments [36–38], theory [18, 20, 39], and simulations [20, 40–42]. Here, we will mainly address computer simulation studies of the polymer dynamics in dilute and semidilute suspensions. Thereby, we want to cover linear polymers and more complex structures such as star polymers and dendrimers. There are other colloidal polymeric structures, e.g., hyperbranched polymers [43] or polymer networks as in microgels. However, far less simulation studies have been performed for such particles, most likely due to the significantly larger number of "monomers" necessary to model the branched structures. There is a wide-range of simulation studies on polymer melts [39, 40, 44, 45] with emphasis on polymer entanglements. The latter aspect goes beyond the scope of this article.

A broad spectrum of simulation approaches have been applied to study the non-equilibrium properties of linear polymers in shear flow. The various techniques are specified, and the respective references are provided in Ref. [46]. More recent studies employing MPC are presented in Refs. [22, 23, 42, 47–51]

3.1. Linear Polymers: Structure and Dynamics in Shear Flow

3.1.1. Structure and Dynamics in Shear Flow

The properties of linear polymers under shear flow have intensively been studied during the last decade by various computer simulation approaches (cf. Ref. [46]). The interest was particularly triggered by experimental studies on DNA molecules, which reveal large conformational changes and an intriguing dynamics [52–55]. Figures 1 and 2 illustrate the monomer density distribution of a polymer and their deformation under flow as obtained from simulations. The polymers are stretched along the flow direction, compressed along the orthogonal directions, and exhibit a preferred orientation with respect to the flow. These properties depend on shear rate in a particular manner and are ultimately linked to the macroscopic rheological behavior of the polymers.

Typically, the extension—specifically in experiments [54, 56]—, the mean square end-to-end distances, or the radius of gyration tensor components along and transverse to the flow direction are considered. The respective longitudinal part increases with increasing shear rate and slowly approaches a maximum, which is smaller than that corresponding to a fully stretched chain [46, 52]. This is a consequence of the continuous end-over-end tumbling dynamics with a non-stationary deformation. The transverse parts decrease with increasing shear rate according to a power law. Similar to convective boundary layers, which occur in the Graetz-Levecque problem in thermal/mass transport where the boundary-layer thickness is governed by a balance of cross-stream diffusion and down-stream convection at high Péclet numbers [57], scaling arguments have been provided for the dependence of the polymer radius of gyration R_{gy} along the gradient direction on the shear rate $\dot{\gamma}$ by balancing monomer convection and diffusion [19, 56, 58]. Typically, the flow strength is characterized by the Weissenberg number $Wi = \dot{\gamma}\tau$, where τ is the longest relaxation time of a polymer. Equating the time for the transverse diffusive transport of a monomer R_{gy}^2/D, where D is the diffusion coefficient, with that of the streamwise active transport over the length scale R_{gx} of the deformed polymer $R_{gx}/(\dot{\gamma}R_{gy})$, leads to [19]

$$R_{gy} \sim \dot{\gamma}^{-1/3}. \tag{2}$$

Thereby, it is assumed that the deformed polymer length is essentially independent of the shear rate. Theory [46] and simulation results [47, 58] confirm the later assumption for large shear rates. An alternative expression is obtained under the assumption that a monomer drags along other monomers, i.e., its diffusion coefficient is reduced by cooperative effects. Setting $D \sim D_0/R_{gy}$, the above considerations yield $R_{gy} \sim \dot{\gamma}^{-1/4}$ [59]. Both power-law dependencies have been observed in simulations [56, 58, 59]. Thereby, the smaller exponent 1/4 is typically seen at smaller shear rates [56, 58, 59] and the larger at high shear rates [19, 58, 59].

An essential aspect for the non-equilibrium shear response is the finite length and inextensibility of a polymer, which is implicitly assumed in the above scaling arguments. Exploiting this fact, the dependence $R_{gy} \sim \dot{\gamma}^{-1/3}$ can be derived theoretically in a different way [46]. For a long and flexible polymer, its mean square radius of gyration is related to the longest relaxation time τ via $R_{gy}^2 \sim \tau$. The inextensibility constraint links the various spatial components of the polymer [46], which implies

$$\tau(1 + \dot{\gamma}^2\tau^2) = const. \tag{3}$$

The quadratic dependence on the shear rate naturally appears even in a lowest order perturbation theory for the polymer deformation along the flow direction, because $\boldsymbol{R}_g^2$ is independent

of the direction of shear. Hence, $\tau \sim \dot{\gamma}^{-2/3}$, or $R_{gy} \sim \dot{\gamma}^{-1/3}$. The full theoretical expression indicates a slow cross-over from an unperturbed polymer to the asymptotic behavior (2) at large shear rates. Thereby, an intermediate regime can be approximated by the relation $R_{gy} \sim \dot{\gamma}^{-1/4}$ over a small range of R_{gy} values. Here, very accurate experiments and simulations are required to separate the various scaling regimes or support the gradual change of R_{gy}.

The preferred alignment angle can be calculated by the components of the radius of gyration tensor, which yields in the asymptotic limit of large shear rates the dependence $\dot{\gamma}^{-1/3}$ [46]. This is confirmed by simulations [47].

First direct experimental observations of the tumbling dynamics of DNA molecules have been presented in Ref. [56]. Various attempts have been undertaken to characterize the tumbling motion by a characteristic tumbling time τ_T and to find the respective shear-rate dependence (cf. Ref. [48, 50]). Simulations and experiments provide a reasonable estimate of τ_T by direct counting of end-over-end tumbling events [54, 56]. Alternatively, power spectral densities (PSD) have been determined for various correlation functions, which yield the sublinear dependence $\tau_T \sim \dot{\gamma}^{-2/3}$ [47, 54, 58, 60–62]. This is consistent with the results obtained by counting tumbling events, as long as thermal motion is important [54, 62]. In the athermal limit, a linear dependence on the shear rate is observed [62], in agreement with expectations for Jeffrey orbits [63]. Various other correlation functions have been considered, involving fluctuations of extensions along the shear and gradient directions [54, 56, 60, 61] or those of the radius of gyration tensor components along these axes [48], which provide typically non-periodic functions [48, 50, 54, 56]. Here, the tight linkage of the polymer deformations along the respective spatial directions during a tumbling cycle is important.

Tumbling can also be characterized by the distribution of time intervals between successive tumbling events [55, 64–66]. Various criteria can be applied to distinguish tumbling events, e.g., the time interval between comparable polymer conformations [55] — characterized by the polymer extension —, or that between successive crossings of the end-to-end vector of the shear-vorticity plane or the gradient-vorticity plane [65]. Since the distribution of tumbling events is typically non-Markovian, it can be rather complicated. However, the distributions should decay exponentially for sufficiently long time intervals, where the events are almost independent. From the exponential function, a decay time can then be extracted and identified as tumbling time. A priori, neither the equivalence of the various definitions is evident, nor is it clear that the same tumbling time or even the same dependence on shear rate, at least qualitatively, is obtained. However, recent theoretical calculations [46, 65] and simulations [48–50] suggest that the decay time is closely related to the stationary-state end-to-end-vector relaxation time of a polymer and that the tumbling time exhibits the shear rate dependence $\tau_T \sim \dot{\gamma}^{-2/3}$. The latter follows directly from the above considerations, namely that $\tau_T = \tau$.

Computer simulation studies at extremely high Weissenberg numbers unravel another non-linear phenomenon, where the polymers shrink in size along the flow direction with increasing *Wi* [59, 67, 68]. Thereby, the transverse components approach a constant value. In the presence of hydrodynamics, the effect is attributed to strong hydrodynamic drag forces, which lead to recirculating flows inside a polymer coil and thus to compaction due to entanglement effects [68]. The very large shear rates necessary for compactification are difficult to achieve in experiments, which is the reason why the phenomenon has not been observed so far.

So far, we have mainly addressed flexible polymers. Semiflexible polymers, where the persistence length is comparable with the contour length exhibit additional features. Here, a more or less gradual change of the behavior from that of a flexible to a rodlike polymer is expected with increasing stiffness. Indeed, rods also align with the flow and exhibit a tumbling motion. For the dynamical behavior, however, presence or lacking of thermal noise plays a major role. Athermal rods in shear flow exhibit so-called Jeffrey orbits, with a rotation frequency which depends linearly on shear rate, i.e., the characteristic time is $\tau \sim \dot{\gamma}^{-1}$ [62, 63, 69]. In the presence of noise, however, the same dependence as for flexible polymers is obtained [62]. This has been predicted by theory [46] and is observed in computer simulations [54] and experiments [70]. However, recent theoretical studies suggest the relation $\tau_T \sim \dot{\gamma}^{-3/4}$ for the tumbling time over a broad range of shear rates for semiflexible polymers [71]. According to the above scaling relation, this would also modify the shear thinning behavior. This aspect deserves further studies. So far, investigations of semidilute solutions of semiflexible polymers indicate a non-power-law decay of the viscosity in the shear thinning region [72].

3.1.2. Rheological Properties in Shear Flow

As mentioned before, the average anisotropic shape of a polymer determines its rheological behavior. This is illustrated by the following scaling consideration [19]. The tensile force F_x on the molecule along the flow direction is $F_x \sim \zeta \dot{\gamma} R_{gy}$, with ζ being the friction coefficient. By the virial theorem, the stress tensor is given by $\sigma_{xy} \sim F_x R_{gy}$, and hence the viscosity by

$$\eta = \sigma_{xy}/\dot{\gamma} \sim R_{gy}^2 \sim \dot{\gamma}^{-2/3} \tag{4}$$

in the asymptotic limit of large shear rates, with the radius of gyration of Eq. (2) [19]. This is consistent with more precise analytical calculations [46] and agrees also with simulation results [19, 58]. Thus, the strong deformation of the polymer leads to pronounced shear thinning, where the shear viscosity decreases by a power-law $\eta \sim \dot{\gamma}^{-\xi}$. Thereby, experiments and simulations [18–20, 39, 46, 47, 55, 58, 73, 74] suggest exponents ranging from $0.4 < \xi < 0.85$ [18], i.e., a broad range of exponents. This is partially explained by the broad crossover between the zero-shear rate plateau and the limiting behavior for $\dot{\gamma} \to \infty$.

The first normal stress coefficient, defined as $\Psi_1 = (\sigma_{xx} - \sigma_{yy})/\dot{\gamma}^2$ [18, 20], can be approximated by $\Psi_1 \sim \sigma_{xx}/\dot{\gamma}^2 \sim F_x R_{gx} \dot{\gamma}^2 \sim R_{gy} R_{gx} \dot{\gamma}$ to derive a scaling relation. As for the derivation of Eq. (3), we set $R_{gy} \sim \tau^{1/2}$ and $R_{gx} \sim \dot{\gamma}\tau^{3/2}$, which leads to

$$\Psi_1 \sim \tau^2 \sim \dot{\gamma}^{-4/3} \tag{5}$$

in agreement with the more precise calculation in Refs. [18, 20, 46]. In contrast to the viscosity, the dependence in Eq. (5) agrees very well with experiments for a broad range of polymer solutions [18, 56, 58] and a wide spectrum of simulations [19, 47, 58, 74]. This could be related to the fact that normal stresses are easier to determine than shear stresses.

The second normal stress coefficient $\Psi_2 = (\sigma_{yy} - \sigma_{zz})/\dot{\gamma}^2$ is determined by hydrodynamic and excluded-volume interactions [18, 20, 47], and hence depends significantly on concentration. For semidilute solutions, our simulations yield the decay $|\Psi_2| \sim Wi_c^{-4/3}$ of the magnitude of Ψ_2 (Ψ_2 is negative) with increasing shear rate, i.e., it decays with the same exponent as Ψ_1 [47]. At low concentrations, we could not extract a clear power-law dependence, since the values of Ψ_2 decrease significantly with decreasing concentration.

We would like to emphasize once more the intimate connection between the structural, dynamical, and rheological properties of flexible polymers in shear flow. The above scaling considerations, and more precise analytical considerations [46], show that all these quantities depend on the relaxation behavior of the polymer, which in turn is determined by the applied shear flow. Hence, here, we established a relation between the microscopic properties of the system and its macroscopic behavior.

At small shear rates, a polymer solution is in the Newtonian regime and the viscosity is independent of $\dot{\gamma}$. However, the zero-shear viscosity η_0 depends on the polymer concentration, which is often presented in the form [47]

$$\eta_0 = \eta_s \left(1 + [\eta] + k_H([\eta c])^2 + \ldots\right). \tag{6}$$

Here, $[\eta]$ is the intrinsic viscosity, c is the polymer concentration, and k_H is the Huggins coefficient [36, 47]. The term $k_H([\eta]c)^2$ depends on hydrodynamic interactions [47]. For flexible polymers, k_H is in the range of $0.2 - 0.8$ and depends on the solvent quality [47]. Typically, the value $k_H = 0.3$ is found experimentally for flexible polymers in good solvents [47]. Figure 3 shows the dependence of the zero-shear viscosity on concentration for polymers of various lengths [47]. The solid line indicates the power-law increase

$$\eta_0 = \eta_s \, (c/c^*)^{1/(3\nu-1)} \tag{7}$$

of η_0 as predicted by a blob model of the polymer [75]. The inset plot depicts the relative viscosity

$$\eta_R = \frac{\eta_0 - \eta_s}{\eta_s [\eta] c} = 1 + k_H [\eta] c + \ldots. \tag{8}$$

The comparison with the simulation data for various polymer lengths yields the coefficient $k_H = 0.35$ [47], which is in close agreement with the experimental result.

Hard sphere suspensions obey the Einstein relation (1). As discussed in Ref. [47], the same relation applies to dilute polymer solutions, when the hydrodynamic radius of a polymer is used to define the volume fraction.

As for dilute systems, a polymer in a semidilute suspension is aligned, deformed, and thus exhibits shear thinning. An example of the polymer contribution to the viscosity is displayed in Fig. 4 for polymers of various lengths N_m and various concentrations. A concentration independent universal behavior

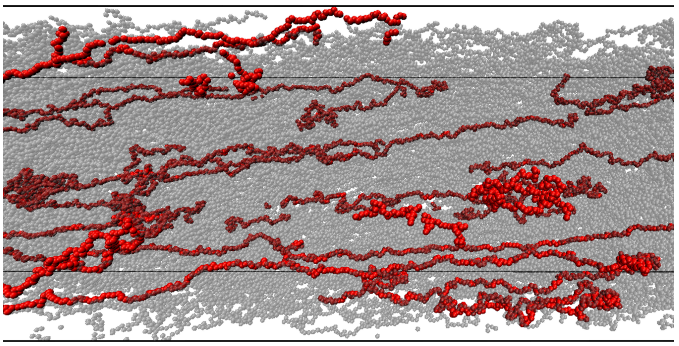

Figure 2: Snapshot of a systems with 800 polymers of length $N_m = 250$ for the Weissenberg number $Wi_c = 184$. For illustration, some of the chains are highlighted in red. From Ref. [48].

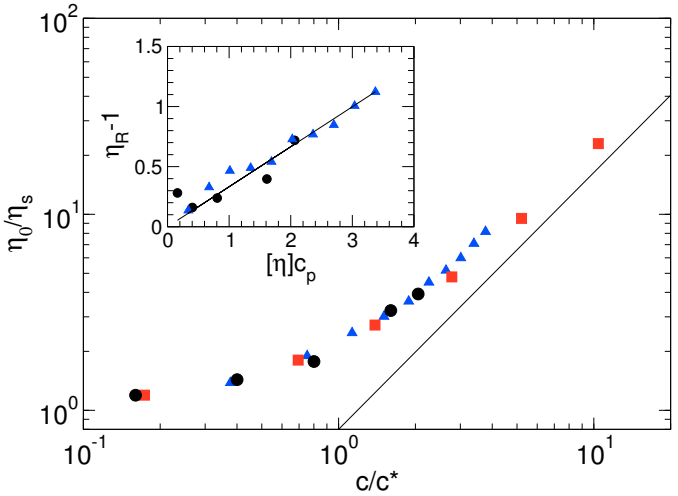

Figure 3: Dependence of the zero-shear viscosity on the scaled concentration c/c^* for the polymer lengths $N_m = 40$ (▲), $N_m = 50$ (●), and $N_m = 250$ (■). The solid line indicates the power-law $(c/c^*)^{1/(3\nu-1)}$ with $\nu = 0.6$. In the inset, $\eta_R - 1$, Eq (7), is shown as function of $[\eta]c$ for $N_m = 40$ (▲) and $N_m = 50$ (●); the slope of the solid line is 0.35, which corresponds to the Huggins constant of polymers in good solvent. From Ref. [47].

is obtained, when the respective quantities are represented as function of the concentration-dependent Weissenberg number $Wi_c = \dot{\gamma}\tau_c$, with the concentration-dependent longest relaxation time τ_c of a polymer. Thus, the same (asymptotic) scaling relations as for a dilute system apply for a semidilute system. A closer look, however, shows that partial screening of hydrodynamic interactions with increasing polymer concentration leads to different relaxation behaviors of the end-to-end vector components along the various spatial directions, where the relaxation times obey $\tau_x \leq \tau_y \leq \tau_z$ [50].

3.2. Star Polymers

Linking polymers at a common center by one of their ends leads to novel polymeric materials with tunable properties. Two extreme limits of such particles are colloidal particles with short grafted polymers, e.g., polymeric latex spheres of varying grafting density [76, 77], or a small connecting center with comparable long polymer arms—star polymers [78, 79]. Here, we

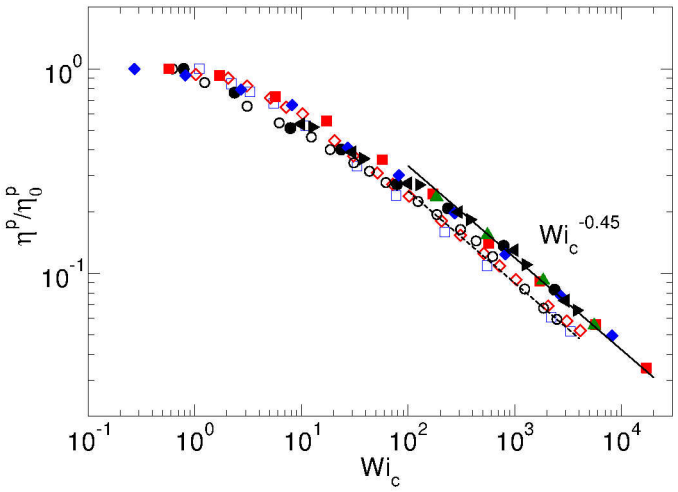

Figure 4: Dependence of the polymer contribution to shear viscosity on Wi_c. Open symbols correspond to systems of polymer length $N_m = 50$ for $c/c^* = 0.16$ (○), $c/c^* = 1.6$ (◇), and $c/c^* = 2.08$ (□). Filled symbols denote results for $N_m = 250$ with the concentration $c/c^* = 0.17$ (●), $c/c^* = 0.35$ (◀), $c/c^* = 1.38$ (▶), $c/c^* = 2.77$ (▲), $c/c^* = 5.19$ (◆), and $c/c^* = 10.38$ (■). From Ref. [47].

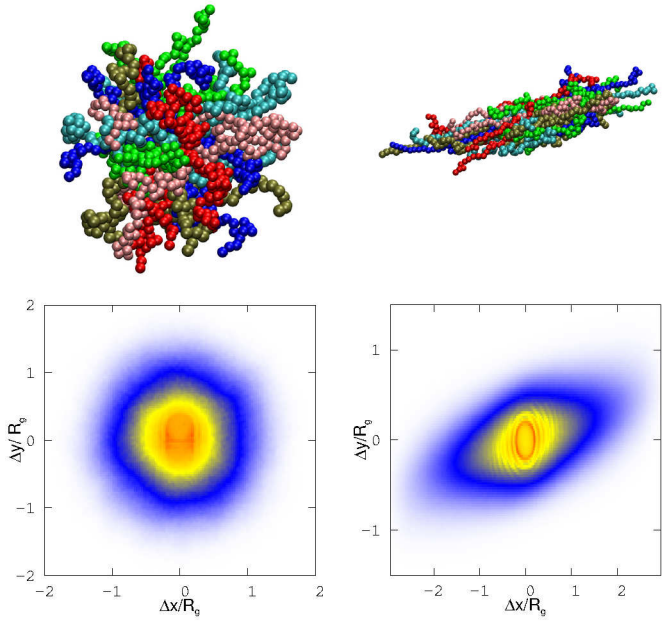

Figure 5: Star polymers conformations (**top**) and monomer density distributions at equilibrium (**left**) and under shear flow (**right**). From Ref. [51].

will focus on star polymers. By varying the arm number (functionality f) and arm length of a star polymer, its properties can be tuned continuously from those of flexible linear polymers to spherical colloidal particles with ultrasoft interactions. Thereby, the structural, dynamical, and rheological properties of star-polymer solutions strongly depend on the arm number, their length, and their concentration c [22, 23, 42, 51, 80–89]. Experimentally, nonequilibrium properties have been considered for a wide range of functionalities and concentrations [76, 90–92].

3.2.1. Structure and Dynamics in Shear Flow

Similar to flexible polymers, shear flow deforms and aligns star polymers as displayed in Figs. 5 and 6 [22, 23, 51, 88]. Individual arms are stretched along the flow direction with increasing shear rate. For a given functionality, we find a universal dependence of the deformation on the concentration-dependent Weissenberg number $Wi_c = \beta(c/c^*)\dot{\gamma}\tau_z$, where $\tau_z \sim N_m^2$ is the Zimm relaxation time and β is a concentration dependent factor [22]. Along the gradient and vorticity directions, star polymers shrink for $Wi_c > 1$. Thereby, the compression along the vorticity direction is quite small compared to that in gradient direction [22, 88]. As expected, the factor $\beta(c/c^*)$ increases strongly with increasing concentration in a nonlinear manner. Thereby, the values for the various functionalities and arm lengths follow a universal curve [22, 23].

We find a universal stretching behavior for stars of various functionalities in terms of a functionality-dependent Weissenberg number $\phi_f Wi_c$ in dilute solution, where the factor ϕ_f accounts for the functionality dependence [23]. At higher concentrations, however, a weaker stretching is observed at large $\phi_f Wi_c$. The radius of gyration tensor component along the gradient direction decays slower with increasing shear rate at higher concentrations. Thereby stars of different functionality exhibit a universal behavior at a particular concentration [23]. Surprisingly, the scale factor ϕ_f decreases with increasing functionality as $\phi_f \sim f^{-2/3}$, i.e., the relaxation time of the shear response decreases with increasing functionality [23]. This is in contrast to the relaxation time of an individual polymer arm, which is predicted to follow the dependence $f^{(2-3\nu)/2}$, with $(2-3\nu)/2 \simeq 0.1$ for $\nu = 0.6$ [81]. A possible explanation for the discrepancy is that the simulation results of [23] are derived for moderate arm lengths and functionalities, while the scaling arguments apply to very long arms and large functionalities. It would certainly be interesting to investigate star-polymer relaxation times in equilibrium in more detail to clarify this problem.

At equilibrium, the arms of a star polymer exhibit conformational properties similar to those of an individual polymer under good solvent conditions. This is reflected in the scaling properties of the arm structure factor, which exhibits the dependence $q^{-1/\nu}$ with $\nu \approx 0.63$ on the scattering vector. Under shear flow, the arms are stretched, which is manifested by an increase of ν up to $\nu \approx 0.8$ for large shear rates [23]. This indicates that the arms are never fully stretched in the ensemble average.

The connectivity of the polymer arms drastically alters the nonequilibrium dynamical behavior of a star polymer. Similar to individual polymers, stars with a few arms only ($f \lesssim 4$) exhibit a tumbling motion, with a cyclic stretching and collapse of the whole star polymer. For large f, however, the stars rather exhibit a tank-treading-like motion [23, 88, 93], reminiscent to the dynamics of vesicles [94–96]. However, individual arms still undergo tumbling motion with a cyclic stretching and collapse of individual arms [51]. The conformational changes are visible in Figs. 5 and 6. Along the vorticity direction, the center-to-end vector correlation function decays exponentially with time, with a shear-rate-dependent relaxation time. The lat-

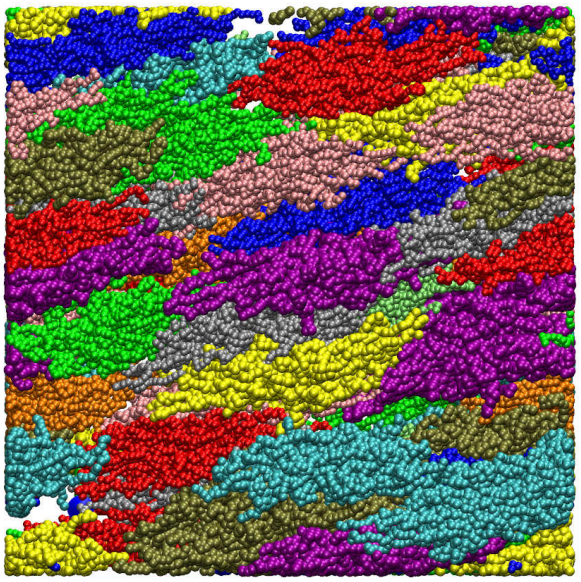

Figure 6: Simulation snapshot of a solution of star polymers with $f = 50$, $c/c^* = 1.46$, and the Weissenberg number $Wi_c \approx 10^2$. Only star polymers with their centers in a slice of thickness of $3R_{g0}$ parallel to the flow-gradient plane are shown, where R_{g0} is the radius of gyration at equilibrium. Multiple colors are used to distinguish the various star polymers more easily. From Ref. [23].

ter scales as $\dot{\gamma}^{-2/3}$ for $Wi_c > 10$, as for linear polymers. Along the shear and gradient directions, the relaxation dynamics is tightly coupled and the respective center-to-end vector component correlation functions exhibit a damped oscillatory behavior [51].

The rotation of the star polymer also affects the fluid flow field. Specifically, the flow lines in the interior of the star polymer are closed, i.e., the internal fluid is screened from the outer one [93]. The rotation dynamics can be quantified by an angular rotation frequency ω_z [23, 88]. For shear rates $\phi_f Wi_c \ll 1$, the frequency assumes the expected value $|\omega_z| = \dot{\gamma}/2$. For large shear rates, the magnitude of the rotation frequency increases as $|\omega_z| \sim \dot{\gamma}^{\zeta}$ with increasing $\dot{\gamma}$. Thereby, the exponent ζ depends strongly on concentration. In dilute solution, we find $\zeta \approx 0$ almost independent of the functionality [23, 88], whereas above the overlap concentration $\zeta \approx 0.35$. Simulations of dilute systems without hydrodynamic interactions yield $\zeta \approx 0.4$ [93]. Thus, the lack or presence of hydrodynamic interactions has a significant influence on the star's rotational dynamics. Qualitatively, an increase of the polymer concentration has the same effect on ω_z as suppression of hydrodynamic interactions. Hence, we interpret the increase of ζ as an indication of screening of hydrodynamic interactions in star polymer solutions at concentrations far above the overlap concentration.

The shear-rate dependence of the rotation frequencies extracted from the simulation data for various functionalities can be reproduced well by the Keller-Skalak model (KS) for vesicles [94] over a broad range of shear rates [23]. Thereby, we identify the axis of the effective ellipsoid with the square root of the respective major axis of the radius of gyration tensor [23].

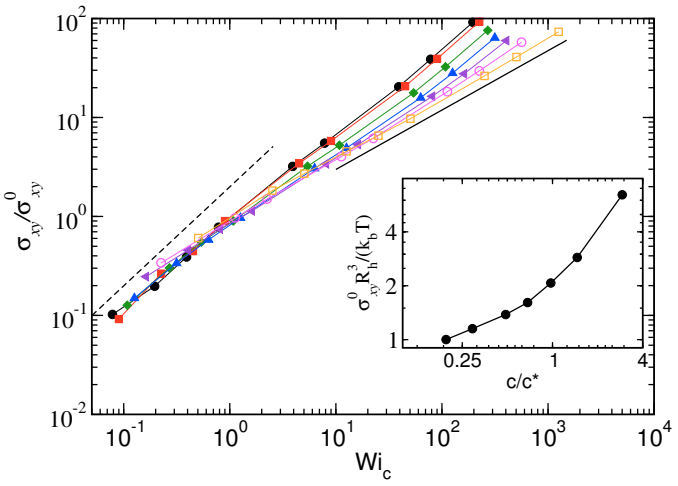

Figure 7: Normalized shear stress σ_{xy} as a function of Wi_c for the concentrations $c/c^* = 0.2$, 0.29, 0.49, 0.68, 0.97, 1.46, 2.92 (top to bottom) and the functionality $f = 50$. The dashed and solid lines indicate the power-laws $\sigma_{xy} \sim Wi_c$ and $\sigma_{xy} \sim Wi_c^{0.6}$, respectively. The inset displays the dependence of the scale factor σ^0_{xy} on concentration, where R_H is the hydrodynamic radius. From Ref. [51].

The diffusive dynamics of the center-of-mass of a star polymer is significantly slowed down with increasing concentration at equilibrium. However, under shear flow, the dynamics is enhanced, and we find diffusion coefficients along the gradient and vorticity direction, which grow by an order of magnitude, when we increase the Weissenberg number from unity to 10^2 [51]. A similar behavior has been reported for the diffusive dynamics of colloidal particles in glasses [97, 98]. At higher concentration, close spatial proximity of the star polymers leads to caging. The respective star polymers rattle in their cage until a certain rearrangement of the neighborhood opens a route to escape. Above the "escape time", the star polymers exhibit Brownian motion. Shear promotes fast and considerable rearrangements of the star polymers, particularly since they are dragged along the flow direction by shear. Thus, the star polymers can escape easily from the local neighborhood, which is reflected in the shear enhanced dynamics.

3.2.2. Rheological Properties in Shear Flow

The flow induced deformation and alignment of star polymers determines the rheological properties of the suspension. Figure 7 illustrates the dependence of the stress tensor on the Weissenberg number and concentration. For $Wi_c > 1$, the shear stress strongly depends on the concentration. The sublinear increase of the shear stress implies shear thinning of the suspension. Simulations reveal a universal dependence of η on $\phi_f Wi_c (> 1)$ for low concentrations to be independent of functionality [51]. Here, the viscosity can be described by the power-law $\eta \sim \dot{\gamma}^{-0.3}$ for $\phi_f Wi_c > 1$. For higher concentrations, again a universal curve is obtained for various functionalities, but with the steeper slope of $\eta \sim \dot{\gamma}^{-0.4}$ [51]. Interestingly, simulations did not show a zero shear-rate plateau for concentrations significantly above the overlap concentration. This points toward the presence of yield stress in such systems.

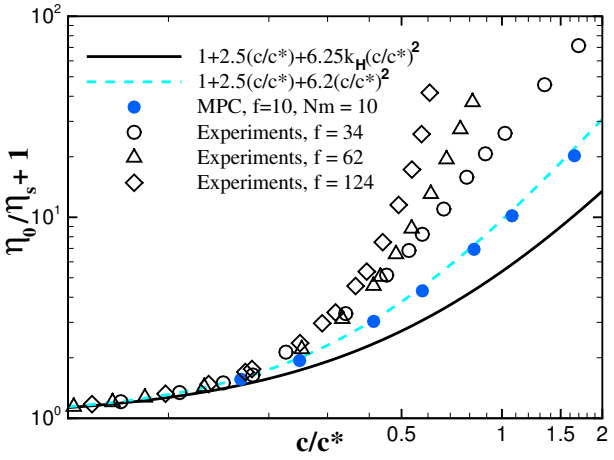

Figure 8: Experimental and simulation results for the zero-shear viscosity of star polymer suspensions. Experimental results (open symbols) for functionalities $f \geq 34$ are extracted from Fig. 6 of Ref. [76]. They are compared with the simulation results for star polymers with $f = 10$ (closed symbols, dashed line) and that for linear polymers [47] (solid line). From Ref. [22].

Zero-shear viscosities η_0 for star polymers of various functionalities from experiments and simulations are displayed in Fig. 8 [76]. The zero-shear viscosity increases rapidly with concentration. The simulation data are well described by the relation $\eta_0/\eta_s = 2.5\phi + 6.2\phi^2$, which implies a faster increase than that for linear polymers, where $\eta_0/\eta_s = 2.5\phi + 6.25k_H\phi^2$ with the Huggins coefficient $k_H \simeq 0.3$ [47]. Furthermore, the zero-shear viscosity as a function of c/c^* depends only very weakly on the arm length. The figure shows a very consistent trend of an increase of the zero-shear viscosity with increasing functionality at constant concentration c/c^*, and demonstrates the crossover of star-polymer properties from ultra-soft to hard-sphere colloids with increasing f. Other simulations yield a near power-law increase of the star-polymer zero-shear rate viscosity in the range $0.1 < c/c^* < 4$ for functionalities in the range $10 \leq f \leq 50$ [51].

The viscosity of star-polymer solutions of very high functionality $f \simeq 390$ has also been measured experimentally at concentrations in the fluid and glassy phases [92]. In the semidilute regime, the shear stress shows a linear increase at low shear rates, followed by a less pronounced growth with an effective exponent of approximately 0.5; this effective exponent decreases with increasing concentration [92]. Both observations are consistent with our simulation results. The exponent of the power law of the shear stress for intermediate Weissenberg numbers is important, because a value larger than unity signals shear banding. Such a behavior has indeed been predicted for concentrated solutions [99]. On the basis of our simulations, no shear banding is predicted for stars with $f \leq 50$ in the investigated concentration range. We expect that considerably larger functionalities are necessary to observe shear banding.

The first normal stress coefficient and the magnitude of the second one decrease with increasing shear rate [42, 51]. Thereby, Ψ_1 exhibits the dependence $\Psi_1 \sim (\phi_f Wi_c)^{-1}$ on the shear rate and functionality ($f \gtrsim 10$). This exponent is different from that of flexible polymers. The reason for the observed difference is yet unexplained. We also find quite pronounced second normal stress coefficients. They decrease as $|\Psi_2| \sim (\phi_f Wi_c)^{-4/3}$ for $\phi_f Wi_c > 1$, i.e., show the same exponent as concentrated polymer solutions. Since excluded-volume interactions mainly determine Ψ_2, the large magnitudes of the second normal stress differences for dilute and concentrated systems point toward strong excluded-volume interactions, both intramolecular at low concentrations, as well as intermolecular at higher concentrations.

3.3. Dendrimers

Dendrimers form another class of ultrasoft colloids with tunable properties [100]. As for star polymers, their dynamical and rheological properties strongly depend on the structural unit, from which the hierarchical entity emerges. However, so far comparably little is known about their rheological properties.

3.3.1. Structure and Dynamics in Flow

Dendrimers are deformed and aligned by a shear flow [101, 102], with a weak compression along the gradient direction and an even weaker effect along the vorticity direction. The elongation in the flow direction depends on the dendrimer rigidity. The simulations of Ref. [101] indicate a power-law increase in the range $0.1 < Wi < 50$, with a slope somewhat smaller than unity. This is in contrast to linear and star polymers, where the elongation increases initially quadratically [23, 47]. Therefore, a suitable relaxation time for the determination of the Weissenberg number seems to be

$$\tau = \frac{\eta l^3 (2G+1)^{3\nu}}{k_B T}, \tag{9}$$

where G is the number of generations, l is the bond length, and $\nu = 0.588$ is the Flory exponent [101].

3.3.2. Rheological Properties

Shear simulations of dendrimers reveal shear thinning at sufficiently high shear rates with an approximate power-law decay $\dot{\gamma}^{-\zeta}$ [43, 102, 103]. For the exponent, the values $\zeta = 1/3$ [103] and $\zeta = 0.55 - 0.6$ [102] have been reported. In Ref. [102], the exponent is found to be independent of topology by comparing linear polymers with dendrimers. The viscosity curves normalized by the zero-shear viscosity for dendrimers and linear polymers collapse as function of the reduced shear rate $[\eta]M\eta_s/(N_A k_B T)\dot{\gamma}$, where M is the molecular weight and N_A is the Avogadro constant.

The dendrimer zero-shear viscosity $[\eta_0]$ exhibits a molecular weight dependence, which is very different from that, e.g., of linear polymers [102, 103]. For a dendrimer, $[\eta_0]$ increases initially at low molecular weight, passes through a maximum, and decreases for a large number of monomers. In contrast, for linear polymers, the viscosity increases in a power-law manner. Shear-thinning of dendrimers has been also found in simulations of elongational flow [43].

The first and second normal stress coefficients also decay for large shear rates with a power-law $|\Psi_{1,2}| \sim \dot{\gamma}^{-4/3}$, similar to star polymers [102].

In general, very little quantitative studies of dendrimer rheology have been performed. This is certainly a consequence of the considerably larger computational cost of simulations due to the required large number of particles.

4. Vesicles, Capsules, and Cells

Droplets, vesicles, capsules and cells are all small bags of an internal fluid, which is separated from the embedding, outside fluid by a closed interface or membrane. The dynamics of such objects, in particular under flow, depends on the physical origin of their deformability, like the surface tension at constant volume for droplets, the membrane bending rigidity at fixed volume and surface-area for vesicles, and, in addition, the membrane shear elasticity for capsules and cells. Therefore, these systems have to be investigated independently to understand the relation between the elasticity of the particles and the rheological behavior of their suspensions.

Suspensions of vesicles, capsules, and cells receive more and more attention due to their importance in technological and biomedical applications. Examples include various cell organelles, drug delivery carriers, cosmetic and food industry applications, tissue components, etc.

4.1. Vesicles

A vesicle consists of a fluidic lipid bilayer membrane of fixed area A, which encloses a fluid volume V. Their shapes and deformations are controlled by the curvature elasticity of the membrane, which is governed by the bending rigidity κ.

In the dilute regime, the vesicle dynamics under shear flow shows three different types of motion: tank-treading (TT), tumbling (TB) and vacillating-breathing (VB) (also called trembling or swinging). In the tank-treading regime, the vesicle shape is stationary, characterized by a constant value of the inclination angle φ of the eigenvector of the radius-of-gyration tensor with the largest eigenvalue and the flow direction, but a rotational motion of a tracer particle attached to the lipid membrane. In the tumbling regime, the whole vesicle rotates, almost like a rigid object. In the vacillating-breathing regime, the shape deformation of the vesicle becomes important, which leads to an oscillation of the shape between a positive and negative inclination angle. The stability of these types of vesicle dynamics depends on viscosity contrast $\lambda = \eta_{in}/\eta_{out}$, where η_{in} and η_{out} are the fluid viscosities of the inner and outer fluids, and shear rate $\dot{\gamma}$, with TT and TB occurring at low and high λ, respectively [94, 104–114].

For tank-treading quasi-spherical vesicles in three dimensions (3D), the viscosity of a dilute suspension has been predicted to be [115, 116]

$$\eta/\eta_{out} = 1 + \frac{5}{2}\Phi\left[1 - \frac{\Delta}{40\pi}(23\lambda + 32)\right] \qquad (10)$$

as a function of excess area $\Delta = 4\pi[(A/(4\pi))(4\pi/(3V))^{2/3} - 1]$ and viscosity contrast λ, where Φ is the vesicle volume fraction.

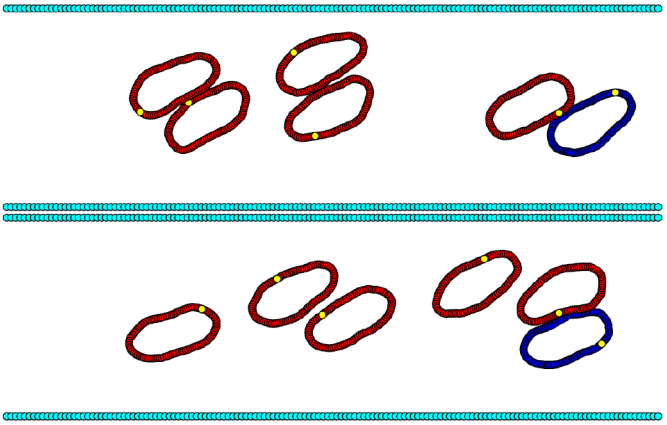

Figure 9: Configurations at consecutive times with time lag $\dot{\gamma}t = 16$ of 2D vesicles with viscosity contrast $\lambda = 1.0$, reduced area $A^* = 0.8$ (the area in units of the area of a circle of equal perimeter length), reduced shear rate $\dot{\gamma}^* = 2.0$, and volume fraction $\Phi = 0.14$. One point of each vesicle membrane is colored yellow for visualization of its evolution during tank-treading, one vesicle blue for visualization of the translational motion. From Ref. [121].

Thus, the intrinsic viscosity $\eta_I = (\eta - \eta_{out})/(\eta_{out}\Phi)$ is predicted to be a decreasing function of Δ and λ. Furthermore, η_I is foreseen to exhibit a cusp-like minimum at the tank-treading to tumbling (or tank-treading to vacillating-breathing) transition, and then to increase again with increasing λ [115, 116]. This latter behavior has been also found in the numerical calculations of a two-dimensional vesicle by the boundary-integral approach [117].

These theoretical predictions have been tested experimentally [118, 119]. While a decrease of η_I with increasing λ was found in Ref. [118], in good agreement with the theoretical prediction in Eq. (10), in contrast, an increase of η_I was observed in Ref. [119]. However, the available experimental results are not conclusive so far for the following reasons. First, vesicle sizes in suspensions are typically polydisperse. Second, viscosity measurements require a minimum volume fraction Φ of vesicles, typically 5% to 10%, and are therefore difficult to extrapolate to the dilute limit [119]. Indeed, recent experiments [120] demonstrate that vesicle interactions become relevant for the suspension's viscosity for Φ around 10%.

This has stimulated new simulation studies of vesicles in shear flow in narrow channels [121–123]. Because of the high numerical cost of vesicle simulations in 3D, these simulations have been performed using 2D model systems. Here, the systems investigated in Ref. [121] and Refs. [122, 123] differ by their presence or absence of thermal fluctuations, which concerns both cross-streamline diffusion as well as membrane undulations.

We discuss first the simulation results for a system with thermal noise. The snapshots of vesicle conformations displayed in Fig. 9 show the typical collision process of two vesicles, which are slightly displaced in the vertical direction, and therefore move with different velocities in the flow direction. As the vesicles collide, their long axes rotate together to align first with the flow direction, possibly a bit further. Then, the

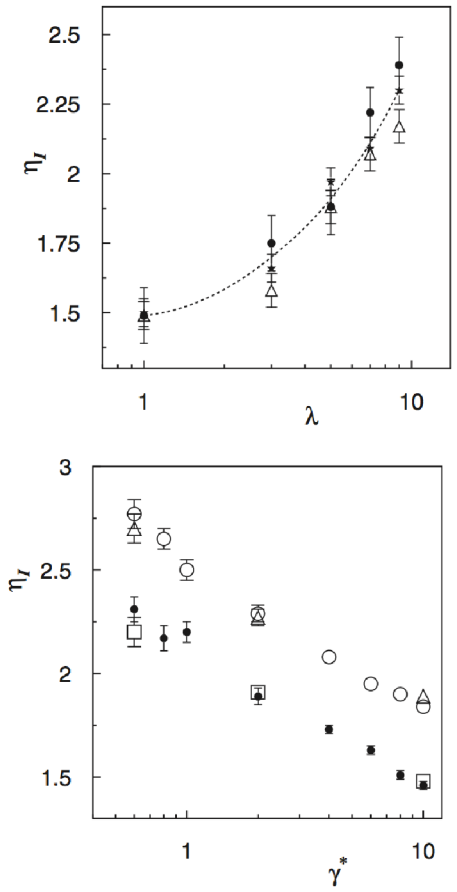

Figure 10: Intrinsic viscosity $\eta_I = (\eta - \eta_{out})/(\eta_{out}\Phi)$ of a vesicle suspension as a function of (**top**) the viscosity contrast λ for reduced shear rate $\gamma^* = 2.0$, reduced area $A^* = 0.8$, and concentrations $\Phi = 0.05$ (•), 0.09 (△), and 0.14 (⋆) (the dashed line is the interpolation to the data, the tank-treading-to-tumbling transition is predicted to occur at $\lambda_c \simeq 3.7$ in the Keller-Skalak (KS) theory [94]); (**bottom**) the reduced shear rate γ^* for reduced area $A^* = 0.8$, concentration $\Phi = 0.28$, and viscosity contrasts $\lambda = 2.0$ (•, □) and 5.0 (○, △). From Ref. [121].

vesicles separate again and the vesicle axis rotates back to its unperturbed inclination angle [121]. This time-dependence obtained in the simulations is in good agreement with experimental results [119]. Similar results have also been obtained from simulations in 3D (without thermal noise) [124]. The intrinsic viscosity of the same system is shown as a function of viscosity contrast and reduced shear rate $\dot{\gamma}^*$ in Fig. 10. Here, the reduced shear rate is defined as $\dot{\gamma}^* = \dot{\gamma} * \tau$, where $\tau = \eta_{out}R_0^3/\kappa$ is the characteristic vesicle relaxation time with average vesicle radius R_0. In the tank-treading regime, the viscosity is found to be an increasing function of λ, in agreement with the experiments of Ref. [119]. Simultaneously, the suspension shows a pronounced shear-thinning behavior, which makes it difficult in the simulation to reach the low-shear-rate plateau [121].

The rheological behavior in the absence of thermal noise seems to be substantially different. In this case, the normalized effective viscosity of the suspension in a 2D narrow channel with $\Phi = 0.06$ is nearly indistinguishable from the viscosity at very high dilution, which decreases with increasing λ [122]. Only in the TB regime with $\lambda \gtrsim 20$, the viscosity of the suspension is significantly enhanced. This effect occurs, because in the steady state TT vesicles order in a single line with approximately the same distances between them. At higher concentrations, vesicles can arrange in two or three files [123]. Simulations of vesicle suspensions in unbounded shear flow in 3D (also without thermal noise) show a very similar dependence on the viscosity contrast for $\Phi = 0.1$ and $\Phi = 0.2$ [124].

If these differences in the rheological behavior can indeed be traced back to the presence or absence of thermal fluctuations, then this raises the important questions (i) of the mechanism which affects the viscosity so strongly, and (ii) in which systems noise plays an important role, and in which not. It has been found in 2D [112] and 3D [109] systems that vesicles have highly convoluted shapes and show an irregular dynamics in and near the vacillating-breathing regime, in agreement with experimental observations [107], which indicates the importance of thermal noise. More detailed studies, both experimental [125] and theoretical [126, 127], show that flow indeed strongly amplifies the effect of thermal fluctuations. In the vacillating-breathing regime, a vesicle finds itself on the edge of a wrinkling instability, where thermally-excited spatial modes are amplified. Fluctuations should be important for low membrane bending rigidities (which increases membrane undulations) and low external fluid viscosity (which increases rotational and translational diffusion coefficients).

Vesicles in capillary flow have also been investigated extensively, in particular using 2D models. Since there is no shear elasticity in 2D (i.e., the membrane is a closed line), the vesicles are also often called red blood cells. We focus here on the rheological behavior in narrow channels. A suspension of discocyte-shaped vesicles is shown to be shear-thinning, in particular near capillary numbers of order unity [128, 129], due to the flow-induced deformation from the discocyte to the parachute shape, and the focusing of the vesicles in the center of the channel. Surprisingly, the predictions for the behavior for small flow velocities differ between 2D and 3D: the eigenvector of the radius-of-gyration tensor with the smallest eigenvalue points in the flow direction in 2D, but is perpendicular to it in 3D. Further work is required to clarify these issues.

4.2. Capsules

Capsules are often referred to particles with an elastic membrane whose area may not be strictly conserved. Thus, capsule deformation in flow may also lead to area dilation. In contrast to vesicles, capsule membrane is elastic. Dynamics of a single capsule in flow has been investigated experimentally [130–132], theoretically [133–135], and in simulations [136–138], while the rheology of capsule suspension has been mainly studied in numerical simulations [26, 139–142].

4.2.1. Dynamics of single capsules

Several authors have studied the flow-induced deformation of synthetic capsules, which consisted of liquid drops surrounded by thin polymeric membranes [130–132, 143]. The experimental results have been fitted with the theory for small capsule

deformations in flow [133] showing good agreement up to moderate capsule deformations. At large deformations a non-linear behavior is expected to have a contribution. More recent experiments on polyamide microcapsules in shear flow [131, 132] have shown shape oscillations and membrane wrinkling. The results have been fitted by the theory [133], even though the theory assumes a steady capsule shape without oscillations. The instability of capsule shape and wrinkling in shear flow has been theoretically investigated in Ref. [134], where a critical shear rate for the instability and the wavelength of wrinkling have been predicted.

Dynamics of capsules in shear flow is also characterized by the two states: tumbling and tank-treading. The transition can be triggered by a viscosity contrast between the inner and outer fluids similar to that for vesicles, which has been first described by the Keller-Skalak theory [94]. The KS theory assumes a fixed path for a tank-treading capsule, and therefore, does not reflect shape oscillations. Improved theories [144, 145] for red blood cells (or also capsules) have added an energy barrier for tank-treading due to membrane elasticity. For a spherical capsule this barrier becomes very small, while it increases as a capsule departs further from a spherical shape. Thus, tumbling-to-tank-treading transition may also depend on the elastic barrier for non-spherical capsules, for instance RBCs. Recent theories [135, 137] have also included membrane oscillations, which appear to be crucial for correct prediction of capsule dynamics. When cell shape deformation is also taken into account, two types of oscillation modes coexist: one induced by the shape deformation similar to fluid vesicles and the other induced by the tank-treading energy barrier [146]. For non-spherical capsules accompanied by a local energy minimum, coupling of these two modes generates a complicated phase behavior.

4.2.2. Rheology of capsule suspensions

The rheology of capsule suspension has been investigated in a number of simulations [26, 139–142] with a common conclusion that capsule suspension exhibits shear thinning. Also, suspension's viscosity strongly depends on the volume fraction of capsules. Rheology of a dilute capsule suspension has been studied in Ref. [139] showing a shear-thinning behavior. However, the dependence of suspension's viscosity on the viscosity ratio (λ) between inner and outer fluids surrounding capsule shows a non-trivial behavior. An initial increase of λ from unity leads to a decrease of the suspension's viscosity, while a further increase in λ may result in an increase of suspension's viscosity. This effect is related to the transition from a tank-treading behavior of capsules to tumbling at high enough values of λ.

The rheology of capsule suspensions at moderate concentrations has been investigated in Refs. [140–142]. Apart from a shear-thinning behavior, microstructure of the suspension have been discussed including also single capsule properties such as orientation and deformation. The measurements of the normal stress differences [140, 141] have shown an unexpected behavior, such that the first normal stress difference is negative at low shear rates and becomes positive as the shear rate is increased. The numerical results of Ref. [141] have also indicated that at high enough concentration of capsules a yield stress may appear even without any aggregation interactions between capsules. The study in Ref. [142] have considered inertial effects on the suspension's rheology in Poiseuille flow. The apparent viscosity of capsule suspension may decrease with an increasing Reynolds number for relatively soft capsules. This effect is related to strong capsule deformations.

4.3. Blood Cells and Blood Flow

Red blood cells (RBCs) combine the properties of both vesicles and capsules with the membrane comprising viscoelastic and area-preserving properties with a finite bending stiffness. Human RBCs have a biconcave shape with a diameter ranging between 6 μm and 8 μm and a thickness of about 2 μm. A RBC membrane is constructed from a lipid bilayer with an attached spectrin-protein cytoskeleton, which provides integrity for a RBC since it is subject to substantial deformations in microcirculatory blood flow. The inner fluid of a RBC is a hemoglobin solution, which can be considered nearly Newtonian and is about 5 times more viscous than the blood plasma.

Mimicking RBC structure, a complete RBC model needs to include elastic energy of the spectrin network, a curvature energy to describe bending resistance of the lipid bilayer, conservation of both the cell area and volume to represent the area incompressibility of the lipid bilayer and incompressibility of a cytosol, membrane viscosity, and the viscosity contrast between the cytosol and blood plasma. The RBC biconcave shape corresponds to the reduced volume $V^* = V_0/(\frac{4}{3}\pi R_0^3)$ with V_0 being the RBC volume and $R_0 = \sqrt{A_0/(4\pi)} = 3.25\ \mu m$, where A_0 is the area of a RBC. The reduced volume of a healthy RBC is equal to about $V^* = 0.6$. More details on RBC and blood flow modeling can be found in recent reviews [147–150].

4.3.1. Shapes and dynamics of single RBCs in flow

The behavior of single RBCs in flow inevitably affects blood rheological properties. Deformation and dynamics of RBCs have been investigated experimentally in various flows including shear flow [145, 151, 152] and tube or Poiseuille flow [153, 154].

Similar to the dynamics described for vesicles and capsules, RBCs in shear flow exhibit tumbling and tank-treading motion [145, 151, 152]. An experimental study [151] has shown that the existence of these two states is due a RBC minimum energy state such that a certain energy barrier has to be exceeded in order for a RBC to tank-tread. Similarly to vesicles and capsules, this transition can be also induced by the viscosity contrast between the cytosol and the suspending fluid, where the latter one is normally varied in experiments. Furthermore, a tank-treading RBC is also subject to a swinging motion around the tank-treading inclination angle [145].

The first theoretical predictions of RBCs dynamics [144, 145] have been derived from the Keller-Skalak theory for vesicles [94] by adding an elastic energy barrier for the tank-treading motion. These theories have qualitatively captured the tumbling-to-tank-treading transition; however, at high enough viscosity contrast ($\lambda \gtrsim 3 - 4$) theoretical predictions led to a relatively wide region of an intermediate dynamics with a co-existence

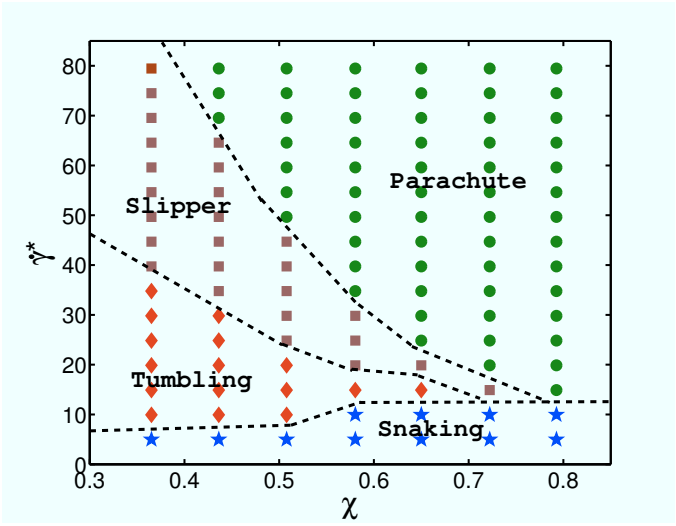

Figure 11: A phase diagram of RBC shapes in tube flow for $Y_r = 18.9 \times 10^{-6}$ N/m, $\kappa_r = 3 \times 10^{-19}$ J, which correspond to average membrane properties of a healthy RBC. Various dynamic states, depending on the flow strength characterized by $\dot{\gamma}^*$ and the confinement χ, are depicted by symbols: parachute (green circles), slipper (brown squares), tumbling (red diamonds) and snaking (blue stars) discocyte. The phase-boundary lines are drawn approximately to guide the eye. From Ref. [161].

of both tumbling and tank-treading states. In contrast, experiments [145, 152] and numerical simulations [30, 31, 34, 146, 155] of RBC dynamics in shear flow have not provided any evidence for the existence of the intermittent region. Recent theories and simulations [135, 137] were able to resolve this issue and found that the prediction of the intermittent region in previous works has been due to the assumption of a fixed tank-treading path of RBCs. Thus, RBCs deformation during tank-treading is important. There also exist breathing dynamics [155] around the tumbling-to-tank-treading transition, which is characterized by strong membrane deformation. Recent experiments [152] and simulations [156] have shown the existence of another dynamical state called rolling, where a RBC just rolls in shear flow with the orientation along the vorticity direction. This transition has been attributed to anisotropic properties of a membrane leading to a rolling state, in which RBC deformations might be reduced. Finally, RBC simulations with a non-zero membrane viscosity [31] have shown that this property might be essential to quantitatively capture RBC dynamics in shear flow.

RBCs in Poiseuille flow show rich behavior characterized by various shapes including parachutes and slippers [28, 30, 33, 153, 154, 157–161]. Parachutes correspond to a symmetric shape similar to a semi-spherical cap which flow in the center of a tube practically without any membrane motion. In contrast, slippers are asymmetric RBCs in tube flow whose membrane is in motion (e.g., tank-treading). There exist two types of slippers observed in experiments, a non-centered slipper [154] and centered slipper [153], where the latter may closely resemble parachute shape. Slipper shapes have been also simulated using 2D models [158, 160] and in 3D [161].

2D simulations in slits [158, 160] have been used to predict a phase diagram of various shapes including parachutes, slippers, and a snaking dynamics, depending on RBC confinement and flow strength. The snaking dynamics is referred to an oscillating RBC dynamics near the tube center. Recent 3D simulations [161] have also resulted in a diagram of RBC shapes in tube flow, which is only qualitatively similar to the diagram in 2D. Figure 11 presents the RBC shape diagram in 3D for different flow rates and confinements. The parachute shape is mainly found at strong confinements and high flow rates, while off-center slippers are predominantly observed at low confinements. At low enough flow rates off-center tumbling RBCs are also found, which are due to the existence of the tumbling-to-tank-treading transition described above. This region is not present in 2D simulations [158, 160], since this transition cannot be captured by a 2D model. At small shear rates $\dot{\gamma}^*$, a snaking region is observed with a RBC performing a periodic oscillatory motion near the center line. However, in contrast to snaking in 2D [158, 160], the snaking motion in 3D is fully three dimensional and may have an orbital drift, which is similar to a RBC rolling motion in shear flow [152, 156]. Another prominent difference between the phase diagrams in Fig. 11 and in 2D simulations [158, 160] is the existence of the "confined slipper" in 2D at high confinements which is absent in 3D. Slippers at high confinements in 3D are suppressed due to the cylindrical shape of a tube, since a confined slipper would have to follow the wall curvature, which is energetically unfavorable.

4.3.2. Blood rheology

Blood rheological characteristics are determined by the properties and dynamics of RBCs due to their high volume fraction or hematocrit. Blood rheology has been measured in a number of experiments [162–164]. Early experiments [162, 165] have found that RBCs in whole blood (i.e., freshly drawn and stabilized against coagulation) are able to aggregate into structures called "rouleaux", which resemble stacks of coins. The aggregation between RBCs is mediated by the plasma proteins [165], which has been verified by an addition of fibrinogen to blood [165]. Rouleaux structures are very fragile and form at rest or at sufficiently slow flows. An increase of shear rate would lead to a break-up of the rouleaux structures resulting eventually in a fully dispersed RBC suspension. The aggregation process is reversible and rouleaux can re-form at low shear rates. Due to aggregation interactions between RBCs, whole blood shows a non-zero yield stress (a threshold stress for flow to begin) [162, 166].

The viscosity of whole blood and of non-aggregating RBC suspension has been measured in experiments [162–164] and modeled in simulations [32, 167]. Figure 12 presents the comparison of the relative viscosity (the RBC suspension viscosity normalized by the viscosity of the suspending media) from simulations and experiments. Blood viscosity exhibits a shear-thinning behavior. A qualitatively similar behavior has been found for capsule suspensions [139, 140] and for a suspension of RBC-like particles [26, 141, 159]. Clearly, a tremendous increase of viscosity at low shear rates is due to the aggregation between RBCs. RBC aggregation has also been investigated for two-cell and multiple-cell aggregates [168, 169] with a focus on

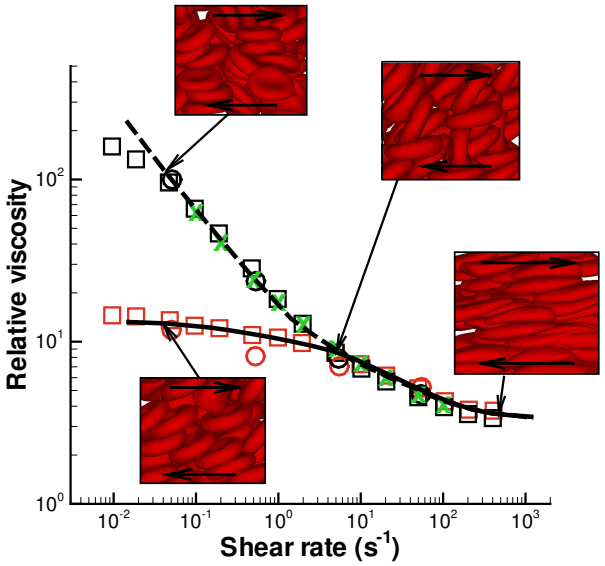

Figure 12: Non-Newtonian relative viscosity (the cell suspension viscosity normalized by plasma viscosity) of whole blood as a function of shear rate at $H_t = 0.45$ and 37^oC: simulation results [167] are shown as black full and dashed lines; experimental data are for: **Whole blood**: green crosses - Merrill et al. [162]; black circles - Chien et al. [163], black squares - Skalak et al. [164]. **Non-aggregating RBC suspension**: red circles - Chien et al. [163]; red squares - Skalak et al. [164]. From Ref. [148].

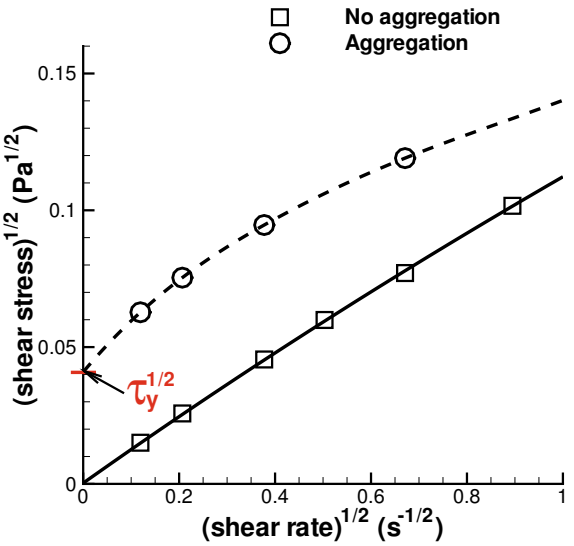

Figure 13: RBC aggregation and yield stress. A Casson plot with a polynomial fit showing the extrapolated intercept τ_y for simulated suspensions with (dashed lines) and without (solid lines) aggregation at $H_t = 0.45$. From Ref. [148].

their behavior in flow. The first attempts to estimate the dependence of viscosity on RBC aggregation [24] were not able to reproduce blood rheology due to a very small simulated system of up to ten aggregated RBCs.

Matching of the viscosity predictions in simulations [167] with the experimental measurements [162–164] allows one to calibrate RBC aggregation interactions. Then, a step further is a direct calculation of aggregation forces between two RBCs, a property which has never been measured in experiments. Simulations [167] predict that the force required for a break-up of two RBCs in the normal direction is in the range of 3.0 pN to 7 pN, while the tangential force needed for a sliding break-up is in the range of 1.5 pN to 3 pN. A fluid shear stress required for RBC disaggregation has been measured in shear flow experiments [170], and lies between 0.01 Pa and 0.1 Pa, while simulations result in a value of about 0.02 Pa.

Existence of a non-zero yield stress in whole blood is attributed to rouleaux structures [162, 166]. A direct confirmation of yield stress is not possible in both experiments and simulations, and therefore, available measurements are usually extrapolated to zero shear rate, which has been done, for example, for blood in Ref. [165]. The extrapolation for soft capsules and cells is often convenient to perform in the Casson coordinates $(\dot{\gamma}^{1/2},\tau_{xy}^{1/2})$, where $\dot{\gamma}$ is the shear rate and τ_{xy} is the shear stress [171]. Figure 13 shows simulated data for $H_t = 0.45$ [167] in Casson coordinates. Extrapolation to zero shear rate clearly results in a non-zero yield stress for whole blood, while for a non-aggregating RBC suspension yield stress vanishes. Simulations [167] predict τ_y to be approximately 0.0017 Pa, while experimental measurements [162] lie between 0.0015 and 0.005 Pa. Yield stress in a RBC suspension may also exist at very high (non-physiological) hematocrit values [141].

The non-Newtonian viscosity and yield stress in blood can be connected to RBC membrane properties, dynamics, and aggregation interactions. Measurements on a single cell level in a RBC suspension may be difficult or unfeasible in experiments, while simulations are ideal for that. The local microstructure of blood can be described by the radial distribution function (RDF) of RBC centers shown in Fig. 14(a) [167]. No significant structures are found for the non-aggregating case, while structures of 2-4 cells can be detected in whole blood for low shear rates. However, any microstructure is completely lost at high shear rates, and therefore the shear-thinning of a non-aggregating RBC suspension is not related to microstructural changes. This also clearly indicates that the aggregation interactions between RBCs are responsible for the steep increase in blood viscosity at low shear rates and for yield stress, since larger rouleaux structures have to be destroyed for blood to flow.

Deformation and dynamics of single RBCs within the suspension is illustrated in Figs. 14(b) and (c) for different shear rates [167]. Tumbling of RBCs at low shear rates is supported by the nearly constant RBC asphericity of about 0.154 (equilibrium value for a discocyte shape) and by the broad orientation-angle (θ) distribution in Fig. 14(c). Also, RBC tumbling is partially hindered in non-aggregating suspensions due to crowding in comparison with the theoretical prediction for tumbling of a single RBC. In contrast, RBC aggregation results in a nearly uniform orientation-angle distribution at low shear rates. At high shear rates, RBCs are subject to tank-treading dynamics supported by a narrow θ distribution in Fig. 14(c). A significant increase of the asphericity in Fig. 14(b) also indicates strong RBC elongation at high shear rates. In the range of shear rates, between 5 s^{-1} and 200 s^{-1}, RBCs strongly deform which is

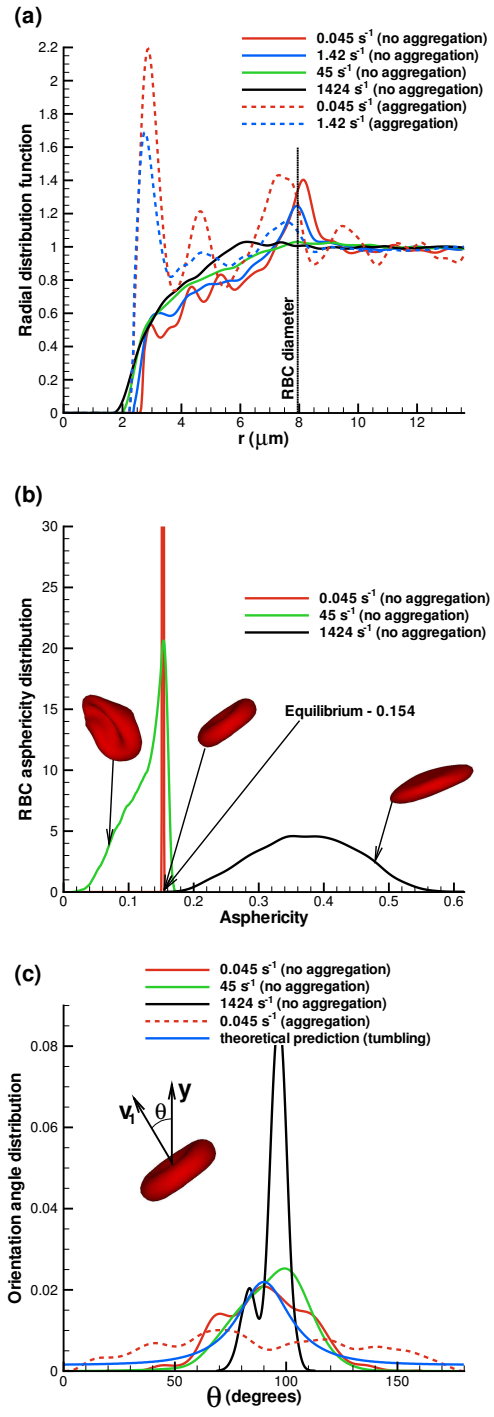

Figure 14: Structural and dynamical properties of RBC suspension at $H_t = 0.45$ with sample snapshots of RBC conformations. (a) RBC suspension's structure characterized by the radial distribution function. (b) RBC asphericity distributions to describe cell deformations through the deviation from a spherical shape. The asphericity is defined as $[(\lambda_1-\lambda_2)^2+(\lambda_2-\lambda_3)^2+(\lambda_3-\lambda_1)^2]/(2R_g^4)$, where $\lambda_1 \le \lambda_2 \le \lambda_3$ are the eigenvalues of the gyration tensor and $R_g^2 = \lambda_1+\lambda_2+\lambda_3$. The asphericity for a RBC in equilibrium is equal to 0.154. (c) Orientational angle distributions for various shear rates. The RBC orientational angle is defined by the angle between the eigenvector V_l of the gyration tensor and the flow-gradient direction (y). The theoretical prediction curve corresponds to the orientational angle distribution of a single tumbling RBC in shear flow calculated using the theory in Ref. [145]. From Ref. [167].

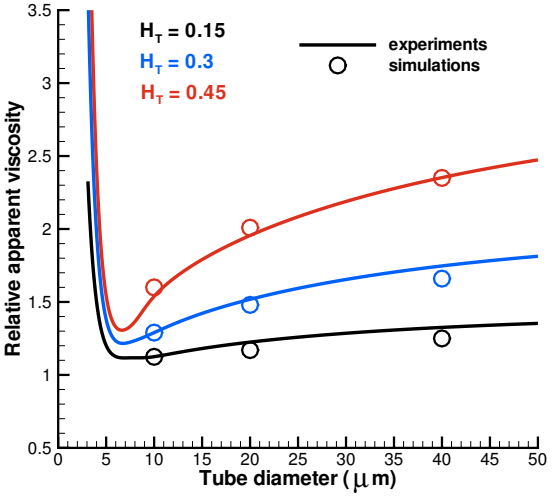

Figure 15: Simulated relative apparent viscosity of blood [174] in comparison with experimental data [173] for different H_T values and tube diameters. From Ref. [148].

indicated by a smaller RBC asphericity than that in equilibrium (Fig. 14(b)). Thus, in this range RBCs attain on average a more spherical shape, which leads to shear thinning through a reduction of shear stresses due to lower tumbling constraints in comparison with the biconcave RBC shape. Moreover, the tumbling-to-tank-treading transition further decreases the shear stresses resulting in shear thinning.

4.3.3. Blood flow

Behavior of RBCs and blood rheological properties govern the flow of blood in microvessels. A well-known effect which describes a dependence of the apparent blood viscosity on vessel diameter is the Fahraeus-Lindqvist effect [172] which predicts a decrease in the effective blood resistance with decreasing tube diameter [173]. The apparent viscosity is found as

$$\eta_{app} = \frac{\pi \Delta P D^4}{128 Q L} = \frac{\Delta P D^2}{32 \bar{v} L}, \tag{11}$$

where D is the tube diameter, Q is the flow rate, and $\Delta P/L$ is the pressure gradient in a tube of length L. For convenience, we normalize the apparent viscosity by the plasma viscosity to obtain relative viscosity of blood as $\eta_{rel} = \eta_{app}/\eta_o$, where η_o is the plasma viscosity. Figure 15 compares simulation results [174] against the empirical fit to experiments [173]. The Fahraeus-Lindqvist effect serves as one of the validation tests for blood flow models, and this test has been also performed in other scientific investigations [25, 35, 175–177].

The Fahraeus-Lindqvist effect arises from the behavior of RBCs in blood flow. In Poiseuille flow, RBCs migrate to the tube center due to a hydrodynamic lift force [178]. The migration of RBCs yields a RBC free layer next to the wall, which effectively can reduce average blood flow resistance (or viscosity). Thus, the thickness of the RBC free layer is directly associated with the Fahraeus-Lindqvist effect. The RBC free layer

has been measured experimentally [179, 180] and in simulations [35, 174–177].

The structure and dynamics of RBCs in blood flow has also been investigated in simulations [33, 176, 177]. In microcapillaries with a diameter comparable with the RBC size, RBCs may have a disordered configuration, form a train of parachutes, or get arranged into a zig-zag structure [33, 181, 182], depending on their concentration and flow rate.

5. Discussion

The considerable amount of work on the dynamics and rheology of soft colloidal particles under flow has revealed both generic and very specific aspects of these systems. For example, two generic aspects are the tank-treading and tumbling motion of individual particles in solution, and the shear-thinning behavior of semi-dilute suspensions. Tank-treading occurs for star polymers, and for vesicles, soft capsules, and red blood cells with small viscosity contrast; tumbling motion is found for linear polymers, and vesicles, stiff capsules, red blood cells with large viscosity contrast. Shear thinning is related to the deformability and alignment of soft particles in flow, and the break-up of aggregates in the case of attractive interactions, and is therefore a property which is shared by all soft-particle suspensions.

However, many properties are quantitatively or qualitatively different, and are very specific for certain systems. For example, the control and variation of the viscosity of the internal fluid of vesicles, capsules and cells has no counterpart in polymeric systems. Therefore, the viscosity contrast can only be employed in the former case to tune rheological properties. A second example is the oscillatory dynamics at the boundary between tank-treading and tumbling, which is found for vesicles, capsules and red blood cells. In the former case, this is related to the dependence of the rotational force on the instantaneous elongation of the particle, while in the latter case it is due to the non-spherical, elastically anisotropic shape of the membrane. This strongly limits the use of vesicle models to describe the behavior of capsules and red blood cells!

However, the dependence of the dynamical and rheological properties of soft particle suspensions on several parameters like the polymer length, polymer stiffness, monomer density within macromolecules, internal viscosity, membrane bending rigidity, membrane shear modulus, particle shape, and particle interactions, offers entirely new possibilities for tuning flow properties. More work is needed in the future to explore the full application potential of these systems. This also requires deeper insights into the relation between microscopic properties and the emergent macroscopic behavior.

References

[1] Einstein A. A new determination of molecular dimensions. Ann Physik 1906;19:289.

[2] Vermant J, Winter H. Special issue devoted to novel trends in rheology. Rheol Acta 2013;52:189. doi:10.1007/s00397-013-0702-x.

[3] McNamara G, Zanetti G. Use of the boltzmann equation to simulate lattice-gas automata. Phys Rev Lett 1988;61:2332.

[4] Shan X, Chen H. Lattice boltzmann model for simulating flows with multiple phases and components. Phys Rev E 1993;47:1815. doi:10.1103/PhysRevE.47.1815.

[5] He X, Luo LS. Theory of the lattice boltzmann method: From the boltzmann equation to the lattice boltzmann equation. Phys Rev E 1997;56:6811. doi:10.1103/PhysRevE.56.6811.

[6] Hoogerbrugge PJ, Koelman JMVA. Simulating microscopic hydrodynamics phenomena with dissipative particle dynamics. Europhys Lett 1992;19:155.

[7] Espanol P, Warren PB. Statistical-mechanics of dissipative particle dynamics. Europhys Lett 1995;30:191.

[8] Espanol P. Hydrodynamics from dissipative particle dynamics. Phys Rev E 1995;52:1734.

[9] Malevanets A, Kapral R. Mesoscopic model for solvent dynamics. J Chem Phys 1999;110:8605.

[10] Kapral R. Multiparticle collision dynamics: Simulation of complex systems on mesoscales. Adv Chem Phys 2008;140:89.

[11] Gompper G, Ihle T, Kroll DM, Winkler RG. Multi-particle collision dynamics: A particle-based mesoscale simulation approach to the hydrodynamics of complex fluids. Adv Polym Sci 2009;221:1. doi:10.1007/978-3-540-87706-6_1.

[12] Bird GA. Molecular Gas Dynamics and the Direct Simulation of Gas Flows. Oxford: Oxford University Press; 1994.

[13] Allahyarov E, Gompper G. Mesoscopic solvent simulations: Multiparticle-collision dynamics of three-dimensional flows. Phys Rev E 2002;66:036702.

[14] Noguchi H, Kikuchi N, Gompper G. Particle-based mesoscale hydrodynamic techniques. EPL 2007;78:10005.

[15] Huang CC, Gompper G, Winkler RG. Hydrodynamic correlations in multiparticle collision dynamics fluids. Phys Rev E 2012;86:056711. doi:10.1103/PhysRevE.86.056711.

[16] Winkler RG, Huang CC. Stress tensors of multiparticle collision dynamics fluids. J Chem Phys 2009;130:074907. doi:10.1063/1.3077860.

[17] Huang CC, Chatterji A, Sutmann G, Gompper G, Winkler RG. Cell-level canonical sampling by velocity scaling for multiparticle collision dynamics simulations. J Comput Phys 2010;229:168. doi:10.1016/j.jcp.2009.09.024.

[18] Bird RB, Curtiss CF, Armstrong RC, Hassager O. Dynamics of Polymer Liquids; vol. 2. New York: John Wiley & Sons; 1987.

[19] Jendrejack RM, de Pablo JJ, Graham MD. Stochastic simulations of DNA in flow: Dynamics and the effects of hydrodynamic interactions. J Chem Phys 2002;116:7752.

[20] Öttinger HC. Stochastic Processes in Polymeric Fluids. Berlin: Springer; 1996.

[21] Mussawisade K, Ripoll M, Winkler RG, Gompper G. Dynamics of polymers in a particle based mesoscopic solvent. J Chem Phys 2005;123:144905. doi:10.1063/1.2041527.

[22] Fedosov DA, Singh SP, Chatterji A, Winkler RG, Gompper G. Semidilute solutions of ultra-soft colloids under shear flow. Soft Matter 2012;8:4109. doi:10.1039/c2sm07009j.
Simulation study of star polymers of low functionality in shear flow using mesoscale methods. Universal aspects in terms of concentration and shear rate are discussed for structural and rheological properties.

[23] Singh SP, Fedosov DA, Chatterji A, Winkler RG, Gompper G. Conformational and dynamical properties of ultra-soft colloids in semi-dilute solutions under shear flow. J Phys: Condens Matter 2012;24:464103. doi:10.1088/0953-8984/24/46/464103.

[24] Liu Y, Liu WK. Rheology of red blood cell aggregation by computer simulation. J Comp Phys 2006;220:139–54.

[25] Doddi SK, Bagchi P. Three-dimensional computational modeling of multiple deformable cells flowing in microvessels. Phys Rev E 2009;79:046318.

[26] MacMeccan RM, Clausen JR, Neitzel GP, Aidun CK. Simulating deformable particle suspensions using a coupled lattice-Boltzmann and finite-element method. J Fluid Mech 2009;618:13–39.

• Of special interest.

⁝ Of outstanding interest.

[27] Gompper G, Kroll DM. Triangulated-surface models of fluctuating membranes. In: Nelson DR, Piran T, Weinberg S, editors. Statistical Mechanics of Membranes and Surfaces; chap. 12. Singapore: World Scientific; 2nd ed.; 2004, p. 359–426.

[28] Noguchi H, Gompper G. Shape transitions of fluid vesicles and red blood cells in capillary flows. Proc Natl Acad Sci USA 2005;102:14159–64.

[29] Dupin MM, Halliday I, Care CM, Alboul L, Munn LL. Modeling the flow of dense suspensions of deformable particles in three dimensions. Phys Rev E 2007;75:066707.

[30] Pivkin IV, Karniadakis GE. Accurate coarse-grained modeling of red blood cells. Phys Rev Lett 2008;101:118105.

[31] Fedosov DA, Caswell B, Karniadakis GE. A multiscale red blood cell model with accurate mechanics, rheology, and dynamics. Biophys J 2010;98:2215–25.
A multiscale membrane model based on a network of springs, which incorporates viscoelastic properties, bending rigidity, and area and volume conservation. The model has been tested against a number of experiments on single red blood cells.

[32] Reasor Jr DA, Clausen JR, Aidun CK. Rheological characterization of cellular blood in shear. J Fluid Mech 2013;726:497–516.
A three-dimensional numerical study of blood rheology. Shear rheology of blood has been investigated including shear-thinning, yield stress, and normal-stress differences.

[33] McWhirter JL, Noguchi H, Gompper G. Flow-induced clustering and alignment of vesicles and red blood cells in microcapillaries. Proc Natl Acad Sci USA 2009;106:6039–43.

[34] Peng Z, Li X, Pivkin IV, Dao M, Karniadakis GE, Suresh S. Lipid bilayer and cytoskeletal interactions in a red blood cell. Proc Natl Acad Sci USA 2013;110:13356–61.
A two layer membrane model representing separately a lipid bilayer and spectrin cytoskeleton of a red blood cell. The model allows for sliding and detachment of the two corresponding layers.

[35] Bagchi P. Mesoscale simulation of blood flow in small vessels. Biophys J 2007;92:1858–77.

[36] Bird RB, Armstrong RC, Hassager O. Dynamics of Polymer Liquids; vol. 1. New York: John Wiley & Sons; 1987.

[37] Chen DT, Wen Q, Janmey PA, Crocker JC, Yodh AG. Rheology of soft materials. Annu Rev Condens Matter Phys 2010;1:301. doi:10.1146/annurev-conmatphys-070909-104120.
Experimental approaches are reviewed, which are suitable for colloids, polymers, and cells. Special emphasis is on non-equilibrium aspects such as shear thinning.

[38] Bent J, Hutchings L, Richards R, Gough T, Spares R, Coates P, et al. Neutron-mapping polymer flow: Scattering, flow visualization, and molecular theory. Science 2003;301:1691.

[39] Rubinstein M, Colby RC. Polymer Physics. Oxford: Oxford University Press; 2003.

[40] Kröger M. Simple models for complex nonequilibrium fluids. Phys Rep 2004;390:453.

[41] Graham MD. Drag reduction in turbulent flow of polymer solutions. Rheology Reviews 2004;2:143.

[42] Winkler RG, Singh SP, Huang CC, Fedosov DA, Mussawisade K, Chatterji A, et al. Mesoscale hydrodynamics simulations of particle suspensions under shear flow: From hard to ultrasoft colloids. Eur Phys J Spec Top 2013;222:2773. doi:10.1140/epjst/e2013-02057-0.

[43] Hajizadeh E, Todd BD, Daivis PJ. Nonequilibrium molecular dynamics simulation of dendrimers and hyperbranched polymer melts undergoing planar elongational flow. J Rheol 2014;58:281.
Numerical investigation of the universal rheological properties of hyperbranched polymers under elongational and shear flow, revealing a strong influence of branching on the shear thinning behavior.

[44] Liu L, Padding JT, den Otter WK, Briels WJ. Coarse-grained simulations of moderately entangled star polyethylene melts. J Chem Phys 2013;138:244912.

[45] Everaers R, Sukumaran SK, Grest GS, Svaneborg C, Sivasubramanian A, Kremer K. Rheology and microscopic topology of entangled polymeric liquids. Science 2004;303:823.

[46] Winkler RG. Conformational and rheological properties of semiflexible polymers in shear flow. J Chem Phys 2010;133:164905. doi:10.1063/1.3497642.
Theoretical investigation of semiflexible polymers in shear flow, linking the polymer dynamics with its shear thinning behavior.

[47] Huang CC, Winkler RG, Sutmann G, Gompper G. Semidilute polymer solutions at equilibrium and under shear flow. Macromolecules 2010;43:10107. doi:10.1021/ma101836x.
Simulation study of polymer suspensions by a mesoscale simulation approach, addressing the universal conformational and rheological properties in terms of shear rate and concentration.

[48] Huang CC, Sutmann G, Gompper G, Winkler RG. Tumbling of polymers in semidilute solution under shear flow. EPL 2011;93:54004. doi:10.1209/0295-5075/93/54004.

[49] Huang CC, Gompper G, Winkler RG. Non-equilibrium properties of semidilute polymer solutions under shear flow. J Phys: Conf Ser 2012;392:012003. doi:10.1088/1742-6596/392/1/012003.

[50] Huang CC, Gompper G, Winkler RG. Non-equilibrium relaxation and tumbling times of polymers in semidilute solution. J Phys: Condens Matter 2012;24:284131. doi:10.1088/0953-8984/24/28/284131.
Simulation study of polymer suspensions by a mesoscale simulation approach. The non-equilibrium relaxation dynamics is analysed and linked to the tumbling behavior.

[51] Singh SP, Chatterji A, Gompper G, Winkler RG. Dynamical and rheological properties of ultrasoft colloids under shear flow. Macromolecules 2013;46:8026. doi:10.1021/ma401571k.
Mesoscale simulation study of star polymers of various functionalities in shear flow addressing universal aspects for structural, dynamical, and rheological properties.

[52] Smith DE, Babcock HP, Chu S. Single-polymer dynamics in steady shear flow. Science 1999;283:1724.

[53] LeDuc P, Haber C, Boa G, Wirtz D. Dynamics of individual flexible polymers in a shear flow. Nature 1999;399:564.

[54] Schroeder CM, Teixeira RE, Shaqfeh ESG, Chu S. Characteristic periodic motion of polymers in shear flow. Phys Rev Lett 2005;95:018301.

[55] Gerashchenko S, Steinberg V. Statistics of tumbling of a single polymer molecule in shear flow. Phys Rev Lett 2006;96:038304.

[56] Teixeira RE, Babcock HP, Shaqfeh ESG, Chu S. Shear thinning and tumbling dynamics of single polymers in the flow-gradient plane. Macromolecules 2005;38:581.

[57] Batchelor GK. An Introduction to Fluid Mechanics. Cambridge: Cambridge University Press; 1990.

[58] Schroeder CM, Teixeira RE, Shaqfeh ESG, Chu S. Dynamics of DNA in the flow-gradient plane of steady shear flow: Observations and simulations. Macromolecules 2005;38:1967.

[59] Dalal SI, Albaugh A, Hoda N, Larson RG. Tumbling and deformation of isolated polymer chains in shearing flow. Macromolecules 2012;45:9493. doi:10.1021/ma3014349.
Numerical analysis of the non-equilibrium conformational and dynamical properties of individual polymers up to extremely high shear rates by Brownian dynamics simulations.

[60] Delgado-Buscalioni R. Cyclic motion of a grafted polymer under shear flow. Phys Rev Lett 2006;96:088303.

[61] Zhang Y, Donev A, Weisgraber T, Alder BJ, Graham MG, de Pablo JJ. Tethered DNA dynamics in shear flow. J Chem Phys 2009;130:234902.

[62] Kobayashi H, Yamamoto R. Tumbling motion of a single chain in shear flow: A crossover from Brownian to non-Brownian behavior. Phys Rev E 2010;81:041807.
Simulation study of the tumbling dynamics of polymers with emphasis on the influence of thermal fluctuations.

[63] Jefferey GB. The motion of ellipsoidal particles immersed in a viscous fluid. Proc R Soc London, Ser A 1922;102:161.

[64] Chertkov M, Kolokolov I, Lebedev A, Turitsyn K. Polymers statistics in a random flow with mean shear. J Fluid Mech 2005;531:251.

[65] Winkler RG. Semiflexible polymers in shear flow. Phys Rev Lett 2006;97:128301. doi:10.1103/PhysRevLett.97.128301.

[66] Usabiaga FB, Delgado-Buscalioni R. Characteristic times of polymer tumbling under shear flow. Macromol Theory Simul 2011;20:466.
Brownian dynamics simulation study of the tumbling dynamics of polymers.

[67] Petera D, Muthukumar M. Brownian dynamics simulation of bead-rod chains under shear with hydrodynamic interaction. J Chem Phys 1999;111:7614.

[68] Sendner C, Netz RR. Single flexible and semiflexible polymers at high

shear: Non-monotonic and non-universal stretching response. Eur Phys J E 2009;30:75.
[69] Dhont JKG, Briels WJ. Rod-Like Brownian Particles in Shear Flow; chap. 3a. Weinheim: Wiley-VCH; 2007, p. 147. doi: 10.1002/9783527617067.ch3b.
[70] Harasim M, Wunderlich B, Peleg O, Kröger M, Bausch AR. Direct observation of the dynamics of semiflexible polymers in shear flow. Phys Rev Lett 2013;110:108302. doi:10.1103/PhysRevLett.110.108302.
[71] Lang PS, Obermayer B, Frey E. Dynamics of a semiflexible polymer or polymer ring in shear flow. Phys Rev E 2014;89:022606.
[72] Huber B, Harasim M, Wunderlich B, Kröger M, Bausch AR. Microscopic origin of the non-Newtonian viscosity of semiflexible polymer solutions in the semidilute regime. ACS Macro Lett 2014;3:136.
Experimental study of the rheological properties of actin filaments in shear flow.
[73] Aust C, Kröger M, Hess S. Structure and dynamics of dilute polymer solutions under shear flow via nonequilibrium molecular dynamics. Macromolecules 1999;32:5660.
[74] Liu T. Flexible polymer chain dynamics and rheological properties in steady flows. J Chem Phys 1989;90:5826.
[75] Raspaud E, Lairez D, Adam M. On the number of blobs per entanglement in semidilute and good solvent solution: Melt influence. Macromolecules 1995;28:927.
[76] Vlassopoulos D, Fytas G, Pakula T, Roovers J. Multiarm star polymers dynamics. J Phys: Condens Matter 2001;13:R855.
[77] Castaing JC, Allain C, Auroy P, Auvray L, Pouchelon A. Nanosized hairy grains: A model system to understand the reinforcement. Europhys Lett 1996;36:153.
[78] Roovers J, Zhou LL, Toporowski PM, van der Zwan M, Iatrou H, Hadjichristidis N. Regular star polymers with 64 and 128 arms. models for polymeric micelles. Macromolecules 1993;26:4324. doi: 10.1021/ma00068a039.
[79] Seghrouchni R, Petekidis G, Vlassopoulos D, Fytas G, Semenov AN, Roovers J, et al. Controlling the dynamics of soft spheres: From polymeric to colloidal behavior. Europhys Lett 1998;42:271.
[80] Grest GS, Kremer K, Witten TA. Structure of many-arm star polymers: A molecular dynamics simulation. Macromolecules 1987;20:1376.
[81] Grest GS, Kremer K, Milner ST, Witten TA. Relaxation of self-entangled many-arm star polymers. Macromolecules 1989;22:1904.
[82] Likos CN, Löwen H, Watzlawek M, Abbas B, Jucknischke O, Allgaier J, et al. Star polymers viewed as ultrasoft colloidal particles. Phys Rev Lett 1998;80:4450.
[83] Jusufi A, Watzlawek M, Löwen H. Effective interaction between star polymers. Macromolecules 1999;32:4470.
[84] Likos CN. Effective interactions in soft condensed matter physics. Phys Rep 2001;348:267.
[85] Fetters LJ, Kiss AD, Pearson DS, Quack GF, Vitus FJ. Rheological behavior of star-shaped polymers. Macromolecules 1993;26:647.
[86] Stellbrink J, Lonetti B, Rother G, Willner L, Richter D. Shear induced structures of soft colloids: Rheo-SANS experiments on kinetically frozen PEP-PEO diblock copolymer micelles. J Phys: Condens Matter 2008;20:404206.
[87] Vlassopoulos D, Fytas G. From polymers to colloids: Engineering the dynamic properties of hairy particles. Adv Polym Sci 2010;236:1.
Review of the structural, dynamical, and rheological properties of star polymers.
[88] Ripoll M, Winkler RG, Gompper G. Star polymers in shear flow. Phys Rev Lett 2006;96:188302. doi:10.1103/PhysRevLett.96.188302.
[89] Gupta S, Kundu SK, Stellbrink J, Willner L, Richter D. Advanced rheological characterization of soft colloidal model systems. J Phys: Condens Matter 2012;24:464102.
[90] Pakula T, Vlassopoulos D, Fytas G, Roovers J. Structure and dynamics of melts of multiarm polymer stars. Macromolecules 1998;31:8931.
[91] Helgeson ME, Wagner NJ, Vlassopoulos D. Viscoelasticity and shear melting of colloidal star polymer glasses. J Rheol 2007;51:297.
[92] Erwin BM, Cloitre M, Gauthierd M, Vlassopoulos D. Dynamics and rheology of colloidal star polymers. Soft Matter 2010;6:2825.
[93] Ripoll M, Winkler RG, Gompper G. Hydrodynamic screening of star polymers in shear flow. Eur Phys J E 2007;23:349. doi: 10.1140/epje/i2006-10220-0.
[94] Keller SR, Skalak R. Motion of a tank-treading ellipsoidal particle in a shear flow. J Fluid Mech 1982;120:27.
[95] Kantsler V, Steinberg V. Orientation and dynamics of a vesicle in tank-treading motion in shear flow. Phys Rev Lett 2005;95:258101. doi: 10.1103/PhysRevLett.95.258101.
[96] Noguchi H, Gompper G. Swinging and tumbling of fluid vesicles in shear flow. Phys Rev Lett 2007;98:128103. doi: 10.1103/PhysRevLett.98.128103.
[97] Krüger M, Weysser F, Fuchs M. Tagged-particle motion in glassy systems under shear: Comparison of mode coupling theory and Brownian Dynamics simulations. Eur Phys J E 2011;34:88.
[98] Harrer CJ, Winter D, Horbach J, Fuchs M, Voigtmann T. Force-induced diffusion in microrheology. J Phys: Condens Matter 2012;24:464105.
[99] Briels WJ, Vlassopoulos D, Kang K, Dhont JKG. Constitutive equations for the flow behavior of entangled polymeric systems: Application to star polymers. J Chem Phys 2011;134:124901.
[100] Ballauff M, Likos CN. Dendrimers in solution: Insight from theory and simulation. Angew Chem Int Ed 2004;43:2998. doi: 10.1002/anie.200300602.
[101] Nikoubashman A, Likos CN. Branched polymers under shear. Macromolecules 2010;43:1610.
The universal conformational properties of model dendrimers are studied by mesoscale simulations.
[102] Bosko JT, Ravi Prakash J. Effect of molecular topology on the transport properties of dendrimers in dilute solution at temperature: A Brownian dynamics study. J Chem Phys 2008;128:034902.
[103] Lyulin AV, Davies GR, Adolf DB. Brownian dynamics simulations of dendrimers under shear flow. Macromolecules 2000;33:3294.
[104] Noguchi H, Gompper G. Fluid vesicles with viscous membranes in shear flow. Phys Rev Lett 2004;93:258102. doi: 10.1103/PhysRevLett.93.258102.
[105] Noguchi H, Gompper G. Dynamics of fluid vesicles in shear flow: Effect of membrane viscosity and thermal fluctuations. Phys Rev E 2005;72:011901. doi:10.1103/PhysRevE.72.011901.
[106] Kantsler V, Steinberg V. Orientation and dynamics of a vesicle in tank-treading motion in shear flow. Phys Rev Lett 2005;95:258101.
[107] Kantsler V, Steinberg V. Transition to tumbling and two regimes of tumbling motion of a vesicle in shear flow. Phys Rev Lett 2006;96:036001.
[108] Misbah C. Vacillating breathing and tumbling of vesicles under shear flow. Phys Rev Lett 2006;96:028104.
[109] Noguchi H, Gompper G. Swinging and tumbling of fluid vesicles in shear flow. Phys Rev Lett 2007;98:128103. doi: 10.1103/PhysRevLett.98.128103.
[110] Lebedev VV, Turitsyn KS, Vergeles SS. Dynamics of nearly spherical vesicles in an external flow. Phys Rev Lett 2007;99:218101.
[111] Vlahovska PM, Gracia RS. Dynamics of a viscous vesicle in linear flows. Phys Rev E 2007;75:016313.
[112] Messlinger S, Schmidt B, Noguchi H, Gompper G. Dynamical regimes and hydrodynamic lift of viscous vesicles under shear. Phys Rev E 2009;80:011901. doi:10.1103/PhysRevE.80.011901.
[113] Zhao H, Shaqfeh ESG. The dynamics of a vesicle in simple shear flow. J Fluid Mech 2011;674:578–604.
[114] Abreu D, Levant M, Steinberg V, Seifert U. Fluid vesicles in flow. Adv Colloid Interface Sci 2014;208:129–41.
A comprehensive review of the dynamics of fluid vesicles in shear and capillary flow, with emphasis on tumbling, tank-treading, trembling and wrinkling of single vesicles.
[115] Danker G, Misbah C. Rheology of a dilute suspension of vesicles. Phys Rev Lett 2007;98:088104.
[116] Danker G, Biben T, Podgorski T, Verdier C, Misbah C. Dynamics and rheology of a dilute suspension of vesicles: Higher-order theory. Phys Rev E 2007;76:041905.
[117] Ghigliotti G, Biben T, Misbah C. Rheology of a dilute two-dimensional suspension of vesicles. J Fluid Mech 2010;653:489.
[118] Vitkova V, Mader MA, Polack B, Misbah C, Podgorski T. Micro-macro link in rheology of erythrocyte and vesicle suspensions. Biophys J 2008;95:L33–5.
[119] Kantsler V, Segre E, Steinberg V. Dynamics of interacting vesicles and rheology of vesicle suspension in shear flow. EPL 2008;82:58005.
[120] Levant M, Deschamps J, Afik E, Steinberg V. Characteristic spatial scale of vesicle pair interactions in a plane linear flow. Phys Rev E 2012;85:056306.

Experimental study of the interplay of thermal membrane fluctuations, trembling dynamics, and flow-induced wrinkling.

[121] Lamura A, Gompper G. Dynamics and rheology of vesicle suspensions in wall-bounded shear flow. EPL 2013;102:28004. doi:10.1209/0295-5075/102/28004.
Numerical study of two-dimensional vesicle suspension in shear flow, using mesoscale hydrodynamics simulations to investigate vesicle interactions in the presence of thermal noise.

[122] Thiébaud M, Misbah C. Rheology of a vesicle suspension with finite concentration: A numerical study. Phys Rev E 2013;88:062707.

[123] Thiébaud M, Shen Z, Harting J, Misbah C. Prediction of anomalous blood viscosity in confined shear flow. Phys Rev Lett 2014;112:238304.

[124] Zhao H, Shaqfeh ESG. The dynamics of a non-dilute vesicle suspension in a simple shear flow. J Fluid Mech 2013;725:709–31.
Numerical study using the boundary-integral method in three dimensions of vesicle suspension in shear flow to investigate vesicle dynamics and interactions, as well as rheology, in the absence of thermal noise.

[125] Levant M, Steinberg V. Amplification of thermal noise by vesicle dynamics. Phys Rev Lett 2012;109:268103.

[126] Abreu D, Seifert U. Effect of thermal noise on vesicles and capsules in shear flow. Phys Rev E 2012;86:010902(R).

[127] Abreu D, Seifert U. Noisy nonlinear dynamics of vesicles in flow. Phys Rev Lett 2013;110:238103.
Theoretical study of quasi-spherical vesicles in shear flow close to the tumbling-to-tank-treading transition, which shows strong sensitivity to the thermal fluctuations.

[128] Lázaro GR, Hernández-Machadoa A, Pagonabarraga I. Rheology of red blood cells under flow in highly confined microchannels: I. effect of elasticity. Soft Matter 2014;10:7195–206.

[129] Lázaro GR, Hernández-Machadoa A, Pagonabarraga I. Rheology of red blood cells under flow in highly confined microchannels. ii. effect of focusing and confinement. Soft Matter 2014;10:7207–17.

[130] Chang KS, Olbricht WL. Experimental studies of the deformation and breakup of a synthetic capsule in steady and unsteady simple shear flow. J Fluid Mech 1993;250:609–33.

[131] Walter A, Rehage H, Leonhard H. Shear-induced deformations of polyamide microcapsules. Colloid Polym Sci 2000;278:169–75.

[132] Walter A, Rehage H, Leonhard H. Shear induced deformation of microcapsules: shape oscillations and membrane folding. Colloid Surf A: Physicochem Eng Aspects 2001;183-185:123–32.

[133] Barthés-Biesel D. Mechanics of encapsulated droplets. Progr Colloid Polym Sci 1998;111:58–64.

[134] Finken R, Seifert U. Wrinkling of microcapsules in shear flow. J Phys: Condens Matter 2006;18:L185–91.

[135] Vlahovska PM, Young YN, Danker G, Misbah C. Dynamics of a non-spherical microcapsule with incompressible interface in shear flow. J Fluid Mech 2011;678:221–47.
A theory for capsule dynamics in shear flow. The analysis takes into account the membrane fluidity, area-incompressibility, and bending resistance.

[136] Ramanujan S, Pozrikidis C. Deformation of liquid capsules enclosed by elastic membranes in simple shear flow: large deformations and the effect of fluid viscosities. J Fluid Mech 1998;361:117–43.

[137] Finken R, Kessler S, Seifert U. Micro-capsules in shear flow. J Phys: Condens Matter 2011;23:184113.

[138] Lac E, Barthés-Biesel D. Deformation of a capsule in simple shear flow: effect of membrane prestress. Phys Fluids 2005;17:072105.

[139] Bagchi P, Kalluri RM. Dynamic rheology of a dilute suspension of elastic capsules: effect of capsule tank-treading, swinging and tumbling. J Fluid Mech 2011;669:498–526.
A numerical study of rheology of a dilute suspension of capsules. Effects of viscosity ratio between internal and external fluids, shear rate, and surface-area dilatation on the rheology of capsule suspension have been considered.

[140] Clausen JR, Reasor Jr DA, Aidun CK. The rheology and microstructure of concentrated non-colloidal suspensions of deformable capsules. J Fluid Mech 2011;685:202–34.

[141] Gross M, Krüger T, Varnik F. Rheology of dense suspensions of elastic capsules: normal stresses, yield stress, jamming and confinement effects. Soft Matter 2014;10:4360–72.

[142] Krüger T, Kaoui B, Harting J. Interplay of inertia and deformability on rheological properties of a suspension of capsules. J Fluid Mech 2014;751:725–45.
A three-dimensional numerical study of the rheology of capsule suspension, with emphasis on the effects of inertia and capsule deformability. Viscosity and suspension microstructure have been investigated.

[143] Chang KS, Olbricht WL. Experimental studies of the deformation of a synthetic capsule in extensional flow. J Fluid Mech 1993;250:581–608.

[144] Skotheim JM, Secomb TW. Red blood cells and other nonspherical capsules in shear flow: oscillatory dynamics and the tank-treading-to-tumbling transition. Phys Rev Lett 2007;98:078301.

[145] Abkarian M, Faivre M, Viallat A. Swinging of red blood cells under shear flow. Phys Rev Lett 2007;98:188302.

[146] Noguchi H. Dynamic modes of microcapsules in steady shear flow: effects of bending and shear elasticities. Phys Rev E 2010;81:056319.

[147] Li X, Vlahovska PM, Karniadakis GE. Continuum- and particle-based modeling of shapes and dynamics of red blood cells in health and disease. Soft Matter 2013;9:28–37.

[148] Fedosov DA, Noguchi H, Gompper G. Multiscale modeling of blood flow: from single cells to blood rheology. Biomech Model Mechanobiol 2014;13:239–58.
A comprehensive review of modeling single cells and their suspensions in flow, with emphasis on the behavior of red blood cells in flow and on blood flow in health and disease.

[149] Freund JB. Numerical simulation of flowing blood cells. Annu Rev Fluid Mech 2014;46:67–95.
A comprehensive review of modeling red blood cells and blood flow, with emphasis on different methods for modeling fluid flow, cell membrane deformation, and their coupling.

[150] Fedosov DA, Dao M, Karniadakis GE, Suresh S. Computational biorheology of human blood flow in health and disease. Ann Biomed Eng 2014;42:368–87.

[151] Fischer TM. Shape memory of human red blood cells. Biophys J 2004;86:3304–13.

[152] Dupire J, Socol M, Viallat A. Full dynamics of a red blood cell in shear flow. Proc Natl Acad Sci USA 2012;109:20808–13.
An experimental study of red blood cell dynamics in shear flow. The paper describes different dynamic states of a red blood cell including tumbling, tank-treading, and rolling and the transitions between them.

[153] Abkarian M, Faivre M, Horton R, Smistrup K, Best-Popescu CA, Stone HA. Cellular-scale hydrodynamics. Biomed Mater 2008;3:034011.

[154] Tomaiuolo G, Simeone M, Martinelli V, Rotoli B, Guido S. Red blood cell deformation in microconfined flow. Soft Matter 2009;5:3736–40.

[155] Yazdani AZK, Bagchi P. Phase diagram and breathing dynamics of a single red blood cell and a biconcave capsule in dilute shear flow. Phys Rev E 2011;84:026314.

[156] Cordasco D, Bagchi P. Orbital drift of capsules and red blood cells in shear flow. Phys Fluids 2013;25:091902.

[157] Gaehtgens P, Dührssen C, Albrecht KH. Motion, deformation, and interaction of blood cells and plasma during flow through narrow capillary tubes. Blood Cells 1980;6:799–812.

[158] Kaoui B, Tahiri N, Biben T, Ez-Zahraouy H, Benyoussef A, Biros G, et al. Complexity of vesicle microcirculation. Phys Rev E 2011;84:041906.
A two-dimensional numerical study of a red blood cell in Poiseuille flow. The study considers a wide range of flow rates and cell confinements leading to a phase diagram of different shapes including parachutes and slippers.

[159] Reasor Jr DA, Clausen JR, Aidun CK. Coupling the lattice-Boltzmann and spectrin-link methods for the direct numerical simulation of cellular blood flow. Int J Num Meth Fluids 2012;68:767–81.

[160] Tahiri N, Biben T, Ez-Zahraouy H, Benyoussef A, Misbah C. On the problem of slipper shapes of red blood cells in the microvasculature. Microvasc Res 2013;85:40–5.

[161] Fedosov DA, Peltomäki M, Gompper G. Deformation and dynamics of red blood cells in flow through cylindrical microchannels. Soft Matter 2014;10:4258–67.
A three-dimensional numerical study of a red blood cell in Poiseuille flow. The study encompasses a wide range of flow rates, cell confinements and properties resulting in several phase diagrams of red blood cell shapes and its different dynamic states.

[162] Merrill EW, Gilliland ER, Cokelet G, Shin H, Britten A, Wells Jr RE.

Rheology of human blood near and at zero flow. Effects of temperature and hematocrit level. Biophys J 1963;3:199–213.
[163] Chien S, Usami S, Taylor HM, Lundberg JL, Gregersen MI. Effects of hematocrit and plasma proteins on human blood rheology at low shear rates. J Appl Physiol 1966;21:81–7.
[164] Skalak R, Keller SR, Secomb TW. Mechanics of blood flow. J Biomech Eng 1981;103:102–15.
[165] Merrill EW, Gilliland ER, Lee TS, Salzman EW. Blood rheology: effect of fibrinogen deduced by addition. Circ Res 1966;18:437–46.
[166] Copley AL, Huang CR, King RG. Rheogoniometric studies of whole human blood at shear rates from 1,000-0.0009 sec^{-1}. Part I. Experimental findings. Biorheology 1973;10:17–22.
[167] Fedosov DA, Pan W, Caswell B, Gompper G, Karniadakis GE. Predicting human blood viscosity in silico. Proc Natl Acad Sci USA 2011;108:11772–7.
A three-dimensional numerical study of blood rheology. Non-Newtonian viscosity and yield stress of blood have been investigated with the correspondence to the microstructure of red blood cell suspension and dynamics of single cells.
[168] Bagchi P, Johnson PC, Popel AS. Computational fluid dynamic simulation of aggregation of deformable cells in a shear flow. J Biomech Eng 2005;127:1070–80.
[169] Wang T, Pan TW, Xing ZW, Glowinski R. Numerical simulation of rheology of red blood cell rouleaux in microchannels. Phys Rev E 2009;79:041916.
[170] Chien S, Sung LA, Kim S, Burke AM, Usami S. Determination of aggregation force in rouleaux by fluid mechanical technique. Microvasc Res 1977;13:327–33.
[171] Casson N. Rheology of Disperse Systems. New York: Pergamon Press; 1992.
[172] Fåhraeus R, Lindqvist T. The viscosity of the blood in narrow capillary tubes. Am J Phys 1931;96:562–8.
[173] Pries AR, Neuhaus D, Gaehtgens P. Blood viscosity in tube flow: dependence on diameter and hematocrit. Am J Physiol 1992;263:H1770–8.
[174] Fedosov DA, Caswell B, Popel AS, Karniadakis GE. Blood flow and cell-free layer in microvessels. Microcirculation 2010;17:615–28.
[175] Freund JB, Orescanin MM. Cellular flow in a small blood vessel. J Fluid Mech 2011;671:466–90.
A three-dimensional numerical study of blood flow in microtubes. Apparent blood viscosity, the development of red-blood-cell-free layer, and cell deformation in tube flow have been studied.
[176] Alizadehrad D, Imai Y, Nakaaki K, Ishikawa T, Yamaguchi T. Quantification of red blood cell deformation at high-hematocrit blood flow in microvessels. J Biomech 2012;45:2684–9.
[177] Lei H, Fedosov DA, Caswell B, Karniadakis GE. Blood flow in small tubes: quantifying the transition to the non-continuum regime. J Fluid Mech 2013;722:214–39.
[178] Abkarian M, Lartigue C, Viallat A. Tank treading and unbinding of deformable vesicles in shear flow: determination of the lift force. Phys Rev Lett 2002;88:068103.
[179] Maeda N, Suzuki Y, Tanaka J, Tateishi N. Erythrocyte flow and elasticity of microvessels evaluated by marginal cell-free layer and flow resistance. Am J Physiol 1996;271:H2454–61.
[180] Kim S, Kong RL, Popel AS, Intaglietta M, Johnson PC. Temporal and spatial variations of cell-free layer width in arterioles. Am J Physiol 2007;293:H1526–35.
[181] McWhirter JL, Noguchi H, Gompper G. Deformation and clustering of red blood cells in microcapillary flows. Soft Matter 2011;7:10967. doi:10.1039/C1SM05794D.
[182] McWhirter JL, Noguchi H, Gompper G. Ordering and arrangement of deformed red blood cells in flows through microcapillaries. New J Phys 2012;14:085026. doi:10.1088/1367-2630/14/8/085026.